



Analysis of post-buckling and delamination in laminated composite St. Venant–Kirchhoff beams using CZM and layer-wise TSNDT



R.C. Batra*, J. Xiao

Department of Engineering Science and Mechanics, M/C 0219, Virginia Polytechnic Institute and State University, Blacksburg, VA 24061, USA

ARTICLE INFO

Article history:

Available online 1 June 2013

Keywords:

TSNDT
Cohesive zone model
Delamination
Geometric nonlinearities
St. Venant–Kirchhoff material
Buckling

ABSTRACT

A layer-wise third order shear and normal deformable plate/shell theory (TSNDT) incorporating a cohesive zone model (CZM) is used to study the initiation and growth of delamination in straight and curved laminated beams. Upon satisfaction of the delamination criteria at a point on the interface between two layers, displacements there of two abutting points on the interface between the two layers are made discontinuous. Delaminations under mode-I, mode-II and mixed-mode static and transient loadings have been studied. All geometric nonlinearities, including the von Karman nonlinearity, are considered. The material of each layer is assumed to be St. Venant–Kirchhoff for which the second Piola–Kirchhoff stress tensor is a linear function of the Green–St. Venant strain tensor. Example problems studied also include delamination growth during axial buckling of a three-layer beam. It is found that the consideration of inertia forces noticeably delays the buckling load and significantly affects the deformed shape of an axially compressed laminated beam.

© 2013 Elsevier Ltd. All rights reserved.

1. Introduction

Delamination is a common failure mode in sandwich structures because of low values of the interfacial strength. Methods employed to analyze delamination include linear elastic fracture mechanics (LEFM) such as the virtual crack closure technique [1], the strain energy release rate (SERR) or the J-integral [2], the virtual crack extension [3], and the cohesive zone model (CZM) [4]. Critical ingredients of these methods are the delamination initiation and growth criteria. Here we use the CZM mainly because it is easy to implement in software, one can readily compute the energy dissipated during delamination and relate it to the critical SERR and the interfacial strength. In the CZM surface tractions at a point on an interface are expressed as a non-monotonic function of the jump in displacements there with the area under the curve equaling the critical SERR. These functions include cubic/exponential [4], bilinear [5], and trapezoidal [6]. Zou et al. [7] proposed a damage surface by combining the conventional stress-based and fracture mechanics-based criteria for mixed-mode failures. A scalar damage parameter is used to describe softening of the interface due to damage induced by delamination growth in laminated composites. Camanho and Dávila [8] described damage of the interface in terms of the mixed-mode relative displacement. Cohesive elements can be either continuum interface elements [9] or nonlinear

springs connected to the corresponding nodes [10] on the two sides of the interface.

A layer-wise plate/beam theory can correctly predict through-the-thickness distributions of transverse shear and transverse normal stresses, and delamination can be simulated by using the CZM. For example, Allix and Corigliano [11] studied delamination of a laminated composite beam using the CZM and the layer-wise first order shear deformable beam theory (FSDT) considering all geometric nonlinearities. Zhang and Wang [12] incorporated the layer-wise FSDT and the crack closure method to study delamination growth in laminated composites.

Here we use the CZM and the layer-wise third order shear and normal deformable plate/shell theory (TSNDT) to study delamination in laminated composite beams. As shown by Batra and Xiao [13] the TSNDT correctly predicts all components of surface tractions on the interface. All geometric nonlinearities are considered in our formulation, and the initiation and propagation of delamination under mode-I, mode-II and mixed-mode static and dynamic loading are studied. The 2nd Piola–Kirchhoff stress tensor is expressed as a linear function of the Green–St. Venant strain tensor. Thus a materially objective constitutive relation is employed. Computed results are found to agree well with those available in the literature. Significant contributions of the work include studying post-delamination and post-buckling deformations of beams deformed under quasi-static and dynamic loadings.

The rest of the paper is organized as follows. In Section 2 we summarize governing equations, boundary conditions and the CZM. We derive governing equations and boundary conditions

* Corresponding author. Tel.: +1 5402316051; fax: +1 5402314574.

E-mail addresses: rbatra@vt.edu (R.C. Batra), xiaojian@vt.edu (J. Xiao).

for the TSNDT as well as a weak form of governing equations in Section 3. We also briefly review in Section 3 the finite element method (FEM) used to numerically solve the problem. Results for the delamination growth in double cantilever beams (DCBs) under pure and mixed-mode static and transient loads are given in Section 4. The delamination growth in an initially delaminated composite beam under axial compression is also studied in this section. Conclusions of this work are summarized in Section 5.

2. Formulation of the problem

2.1. Brief review of the continuum theory

2.1.1. Kinematics

A schematic sketch of the problem studied is shown in Fig. 1. The position vector of point p in the reference configuration is described by using orthogonal curvilinear coordinate axes y_1, y_2, y_3 in the reference configuration with y_1 -axis along the tangent to the mid-surface of the beam, y_2 -axis pointing into the plane of the paper, and y_3 -axis pointing along the local thickness direction. Let X_1, X_2, X_3 be fixed rectangular Cartesian coordinate axes, and the y_2 -axis be parallel to the X_2 -axis. Let position vectors, with respect to fixed rectangular Cartesian coordinate axes, of point p located at (y_1, y_2, y_3) in the reference configuration be \mathbf{x} and \mathbf{X} in the current and the reference configurations, respectively.

Components, G_{ij} , of the metric tensor in the reference configuration are given by [14]

$$G_{ij} = \mathbf{A}_i \cdot \mathbf{A}_j, \quad \mathbf{A}_i = \frac{\partial \mathbf{X}}{\partial y_i} \quad (1)$$

For orthogonal curvilinear coordinate axes the metric tensor, G_{ij} , is non-zero only when $i = j$. We set

$$H_1 = \sqrt{G_{11}}, \quad H_2 = \sqrt{G_{22}} = 1, \quad H_3 = \sqrt{G_{33}} = 1, \\ \tilde{\mathbf{e}}_i = \frac{\mathbf{A}_i}{H_{(i)}} \text{ (no sum on } i) \quad (2)$$

Here $(\tilde{\mathbf{e}}_1, \tilde{\mathbf{e}}_2, \tilde{\mathbf{e}}_3)$ are unit base vectors along the y_1, y_2 and y_3 axes, respectively, and

$$H_1 = \left(1 + \frac{y_3}{R}\right), \quad \frac{\partial \tilde{\mathbf{e}}_1}{\partial y_1} = -\frac{\tilde{\mathbf{e}}_3}{R}, \quad \frac{\partial \tilde{\mathbf{e}}_3}{\partial y_1} = \frac{\tilde{\mathbf{e}}_1}{R} \quad (3)$$

where R is the radius of curvature at the point (y_1, y_2, y_3) .

We study finite plane strain deformations in the X_1X_3 -plane, and for simplicity assume that the curved beam is given of rectangular cross-section. The displacement \mathbf{u} of point p is given by

$$\mathbf{u} = \mathbf{x} - \mathbf{X} \quad (4)$$

where \mathbf{u} is a function of y_1 and y_3 , and $u_2 = 0$. Physical components of the displacement gradient, \mathbf{F} , are given by [14]

$$[\mathbf{F}] = \begin{bmatrix} 1 + \frac{1}{H_1} \left(\frac{\partial u_1}{\partial y_1} + \frac{u_3}{R} \right) & 0 & \frac{\partial u_1}{\partial y_3} \\ 0 & 1 & 0 \\ \frac{1}{H_1} \left(\frac{\partial u_3}{\partial y_1} - \frac{u_1}{R} \right) & 0 & 1 + \frac{\partial u_3}{\partial y_3} \end{bmatrix} \quad (5)$$

The Green-St. Venant strain tensor, \mathbf{E} , defined by

$$\mathbf{E} = \frac{1}{2} (\mathbf{F}^T \mathbf{F} - \mathbf{1}) \quad (6)$$

where $\mathbf{1}$ is the identity tensor, has following non-zero physical components:

$$E_{11} = \frac{1}{H_1} \left(\frac{\partial u_1}{\partial y_1} + \frac{u_3}{R} \right) + \frac{1}{2H_1^2} \left[\left(\frac{\partial u_1}{\partial y_1} + \frac{u_3}{R} \right)^2 + \left(\frac{\partial u_3}{\partial y_1} - \frac{u_1}{R} \right)^2 \right] \\ E_{33} = \frac{\partial u_3}{\partial y_3} + \frac{1}{2} \left[\left(\frac{\partial u_1}{\partial y_3} \right)^2 + \left(\frac{\partial u_3}{\partial y_3} \right)^2 \right] \\ 2E_{13} = \frac{1}{H_1} \left(\frac{\partial u_3}{\partial y_1} - \frac{u_1}{R} \right) + \frac{\partial u_1}{\partial y_3} + \frac{1}{H_1} \left[\frac{\partial u_3}{\partial y_3} \left(\frac{\partial u_3}{\partial y_1} - \frac{u_1}{R} \right) + \frac{\partial u_1}{\partial y_3} \left(\frac{\partial u_1}{\partial y_1} + \frac{u_3}{R} \right) \right] \quad (7)$$

We note that \mathbf{E} incorporates all geometric nonlinearities including the von Karman nonlinearity, and is valid for finite (or large) deformations of a beam. The strain tensor for infinitesimal deformations is obtained from Eq. (7) by neglecting the nonlinear terms included in brackets.

2.1.2. Kinetics

The in-plane displacements (u_1, u_3) of a point are governed by the following equations expressing the balance of linear momentum written in the Lagrangian description of motion using physical components $T_{11}, T_{13}, T_{31}, T_{33}$, of the first (not necessarily symmetric) Piola–Kirchhoff stress tensor [14], and initial and boundary conditions.

$$\rho_0 \ddot{u}_1 = \frac{1}{H_1} \frac{\partial T_{11}}{\partial y_1} + \frac{1}{H_1} \frac{\partial (H_1 T_{13})}{\partial y_3} + \frac{1}{H_1 R} T_{31} + f_1 \quad (8.a)$$

$$\rho_0 \ddot{u}_3 = \frac{1}{H_1} \frac{\partial T_{31}}{\partial y_1} + \frac{1}{H_1} \frac{\partial (H_1 T_{33})}{\partial y_3} - \frac{1}{H_1 R} T_{11} + f_3 \quad (8.b)$$

$$u_i(y_1, y_3, 0) = u_i^0(y_1, y_3), \quad \dot{u}_i(y_1, y_3, 0) = \dot{u}_i^0(y_1, y_3) \quad (8.c, d)$$

$$T_{ij} N_j^t = \tilde{t}_i(y_1, y_3, t) \text{ on } \Gamma_t, \quad u_i(y_1, y_3, t) = \bar{u}_i(y_1, y_3, t) \text{ on } \Gamma_u \quad (8.e, f)$$

$$T_{ij} N_j^{c+} = \tilde{f}_i^{c+}, T_{ij} N_j^{c-} = \tilde{f}_i^{c-} \text{ on } \Gamma_c \quad (8.g)$$

$$\tilde{f}_1^{c-} = \hat{a}(\mathbb{R}_{11} \sigma_t + \mathbb{R}_{31} \sigma_n), \quad \tilde{f}_3^{c-} = \hat{a}(\mathbb{R}_{13} \sigma_t + \mathbb{R}_{33} \sigma_n), \quad \tilde{f}_i^{c+} = -\tilde{f}_i^{c-} \text{ on } \Gamma_c \quad (8.h)$$

$$[\mathbb{R}] = \begin{bmatrix} \cos \theta & 0 & \sin \theta \\ 0 & 1 & 0 \\ -\sin \theta & 0 & \cos \theta \end{bmatrix} \quad (8.i)$$

In Eq. (8) i and j equal 1 and 3, f_1 and f_3 are components of the body force per unit reference volume along the y_1 - and the y_3 -axes,

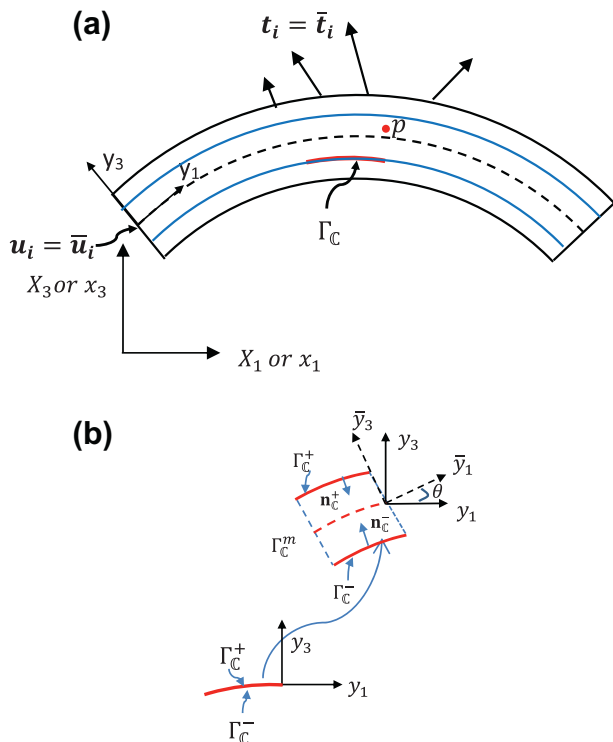


Fig. 1. Schematic sketches of curved beam (a) and of cohesive interface Γ_c (b). X_2, x_2, y_2 - and \bar{y}_2 -axes pointing into the plane of the paper are not shown in the figure.

respectively, ρ_0 the mass density in the reference configuration, and $\hat{u}_i = \frac{\partial^2 u_i}{\partial t^2}$. The initial displacement u_i^0 and the initial velocity \dot{u}_i^0 are known functions of y_1 and y_3 . \mathbf{N}_i is a unit outward normal in the reference configuration at a point on the boundary Γ_t where surface tractions are prescribed as \hat{t}_i . On boundary Γ_u , displacements are prescribed as \hat{u}_i . \mathbf{N}^{\pm} is the outward unit normal on the corresponding interface Γ_c^{\pm} , \hat{a} equals the area into which a unit surface area in the reference configuration is deformed, \mathbb{R}_{ij} the rotation matrix, θ the angle between y_1 - and \bar{y}_1 -axes, \hat{f}_i^{\pm} the traction on the cohesive interface Γ_c^{\pm} , and σ_t and σ_n the tangential and the normal tractions in the current configuration of the cohesive interface. Tractions σ_t and σ_n are related to jumps in displacements on the cohesive interface as discussed in subsection 2.1.4. As outward normals at corresponding points on the upper and the lower surfaces of a cohesive interface may not be parallel to each other, we use a mean cohesive interface Γ_c^m (see Fig. 1) to find surface tractions and jumps in tangential and normal displacements on the cohesive interface. Accordingly, we introduce local coordinate axes \bar{y}_1 and \bar{y}_3 , respectively, along the tangent and the normal to the deformed mean cohesive interface Γ_c^m . The unit outward normal \mathbf{n}_c^{\pm} on Γ_c^{\pm} in the current configuration is found from values of the deformation gradient on the corresponding interface. We assume that the rotation angle θ of the mean cohesive interface Γ_c^m equals the average of the rotation angles of unit normals \mathbf{n}_c^{\pm} . The deformed area \hat{a} of the mean cohesive interface Γ_c^m is taken equal to the average of areas into which unit areas on Γ_c^+ and Γ_c^- are deformed. We note that tractions on Γ_c^+ and Γ_c^- are equal and opposite.

Using the transformation matrix \mathbb{R}_{ij} , the jump displacements δ_t and δ_n , of corresponding points on Γ_c^+ and Γ_c^- are given by

$$\delta_t = \mathbb{R}_{1j} \left(u_j^+(y_1, y_3, t) - u_j^-(y_1, y_3, t) \right) \text{ on } \Gamma_c, \quad j = 1, 3 \quad (9.a)$$

$$\delta_n = \mathbb{R}_{3j} \left(u_j^+(y_1, y_3, t) - u_j^-(y_1, y_3, t) \right) \text{ on } \Gamma_c, \quad j = 1, 3 \quad (9.b)$$

where $u_j^+(y_1, y_3, t)$ and $u_j^-(y_1, y_3, t)$ represent, respectively, displacements of a point on Γ_c^+ and Γ_c^- with respect to y_1 and y_3 coordinate axes, δ_t and δ_n equal jumps in the tangential and the normal displacements of corresponding points on Γ_c^+ and Γ_c^- with respect to \bar{y}_1 and \bar{y}_3 coordinate axes on the mean cohesive interface Γ_c^m .

2.1.3. Constitutive relations

We assume that the beam material is St. Venant–Kirchhoff for which the strain energy density, W , is given by

$$W = \frac{1}{2} E_{ij} C_{ijkl} E_{kl}, \quad C_{ijkl} = C_{klij} = C_{jikl} \quad (10)$$

where \mathbf{C} is the fourth-order elasticity tensor having 21 independent components for three-dimensional deformations of a general anisotropic material. The independent components of \mathbf{C} with respect to the material principal axes reduce to 9, 5 and 2 for an orthotropic, transversely isotropic and isotropic material, respectively. The strain energy density for the St. Venant–Kirchhoff material reduces to that of a Hookean material if the finite strain tensor \mathbf{E} is replaced in Eq. (10) by the strain tensor for infinitesimal deformations. Batra [15] has compared the response of four elastic materials for which a stress tensor is a linear function of an appropriate strain tensor (e.g., the Cauchy stress tensor is a linear function of the Almansi–Hamel strain tensor). For infinitesimal deformations the four constitutive relations give the same stress–strain curve for simple tensile and simple shear deformations, but their predictions for finite deformations are quite different.

For a nonlinear elastic material, physical components of the second Piola–Kirchhoff stress tensor \mathbf{S} are related to \mathbf{E} by

$$S_{ij} = \frac{\partial W}{\partial E_{ij}} = C_{ijkl} E_{kl} \quad (11)$$

However, \mathbf{S} has no physical interpretation. Other stress tensors such as the Cauchy or the 1st Piola–Kirchhoff stress tensor can be derived from \mathbf{S} only if the deformation gradient \mathbf{F} is known [15]. For plane strain deformations of an orthotropic material with the material principal axes coincident with the coordinate axes (y_1, y_2, y_3) , Eq. (11) reduces to

$$\begin{Bmatrix} S_{11} \\ S_{33} \\ S_{13} \end{Bmatrix} = \begin{bmatrix} C_{1111} & C_{1133} & 0 \\ C_{3311} & C_{3333} & 0 \\ 0 & 0 & C_{1313} \end{bmatrix} \begin{Bmatrix} E_{11} \\ E_{33} \\ 2E_{13} \end{Bmatrix} \quad (12.a)$$

$$C_{1111} = \frac{1 - \nu_{23}\nu_{32}}{E_2 E_3 \mathcal{D}}, \quad C_{3333} = \frac{1 - \nu_{12}\nu_{21}}{E_1 E_2 \mathcal{D}},$$

$$C_{1133} = C_{3311} = \frac{\nu_{31} + \nu_{21}\nu_{32}}{E_2 E_3 \mathcal{D}}, \quad C_{1313} = G_{13} \quad (12.b)$$

$$\mathcal{D} = \frac{1}{E_1 E_2 E_3} \begin{vmatrix} 1 & -\nu_{21} & -\nu_{31} \\ -\nu_{12} & 1 & -\nu_{32} \\ -\nu_{13} & -\nu_{23} & 1 \end{vmatrix} \quad (12.c)$$

Here E_1, E_2 and E_3 represent, respectively, Young’s moduli along the y_1 -, the y_2 - and the y_3 -axes, G_{13} is the shear modulus in the $y_1 y_3$ -plane, ν_{12}, ν_{13} and ν_{23} are Poisson’s ratios.

Recalling that [15]

$$\mathbf{T} = \mathbf{F}\mathbf{S} \quad (13)$$

where \mathbf{T} is the 1st Piola–Kirchhoff stress tensor, we get

$$\begin{bmatrix} T_{11} & T_{13} \\ T_{31} & T_{33} \end{bmatrix} = \begin{bmatrix} F_{11}S_{11} + F_{13}S_{13} & F_{11}S_{13} + F_{13}S_{33} \\ F_{31}S_{11} + F_{33}S_{13} & F_{31}S_{13} + F_{33}S_{33} \end{bmatrix} \quad (14)$$

Substitution for \mathbf{F} from Eq. (5) into Eq. (14), for \mathbf{E} from Eq. (7) into Eq. (12) and the result into Eq. (14) gives expressions for \mathbf{T} in terms of displacements u_1 and u_3 and the four elastic constants $C_{1111}, C_{1133}, C_{3333}$, and C_{1313} . Even though components of \mathbf{S} are quadratic in displacement gradients those of \mathbf{T} are cubic in displacement gradients. We note that constitutive relations (11) and (13) are materially objective, i.e., are invariant under a rigid body motion superimposed upon the present configuration.

The true stress or the Cauchy stress, $\boldsymbol{\sigma}$, is related to the 1st Piola–Kirchhoff stress by [15]

$$\boldsymbol{\sigma} = \frac{1}{J} \mathbf{T}\mathbf{F}^T, \quad (15)$$

where J is the determinant of the deformation gradient \mathbf{F} . Thus $\boldsymbol{\sigma}$ need not be a polynomial function of the displacement gradients.

We now substitute for \mathbf{T} into Eq. (8), and solve the resulting nonlinear coupled partial differential equations (PDEs) for u_1 and u_3 under pertinent initial and boundary conditions. These PDEs involve second-order derivatives of u_1 and u_3 with respect to y_1 and y_3 and time t .

2.1.4. Cohesive zone model

2.1.4.1. Mode-I or mode-II deformations. We first describe the CZM for mode-I and mode-II deformations, and then for mixed-mode deformations. We postulate the traction–separation relations depicted in Fig. 2a and b for mode-I and mode-II deformations, respectively. For relative normal (tangential) displacement $\delta_n(\delta_t)$ of adjoining points on the two sides of the interface less than $\delta_n^0(\delta_t^0)$ corresponding to point A in Fig. 2a (Fig. 2b), the traction–separation relation represented by straight line OA is completely reversible. For monotonically increasing values of $\delta_n(\delta_t)$ greater than $\delta_n^0(\delta_t^0)$ the traction–separation relation is given by straight line AB. For $\delta_n = \delta_n^f(\delta_t = \delta_t^f)$ there is complete separation (sliding) at the interface for mode-I (mode-II) deformations. For mode-I

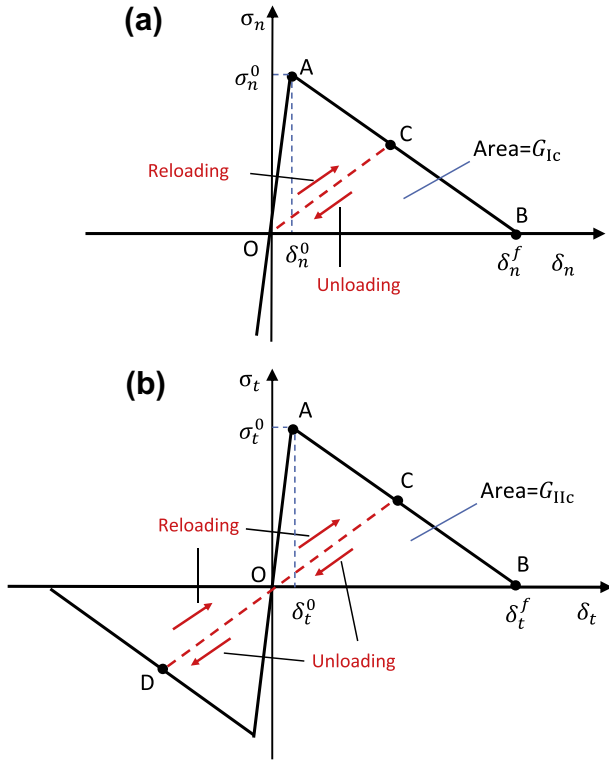


Fig. 2. Traction–separation relations at cohesive interface; (a) Mode-I, (b) Mode-II.

deformations, the separated surfaces are traction free and for mode-II deformations the sliding surfaces are assumed to be smooth or frictionless. Should the relative displacement $\delta_n(\delta_t)$ exceeding $\delta_n^0(\delta_t^0)$ but less than $\delta_n^f(\delta_t^f)$ begin to decrease, then the traction–separation relation follows the path CO for δ_n and COD for δ_t . The area of the triangle OAB equals the critical strain energy release rate G_{Ic} (G_{IIc}) for mode-I (mode-II) deformations.

Values of G_{Ic} (G_{IIc}) and $\sigma_n^0(\sigma_t^0)$ characterize the interface. Here $\sigma_n^0(\sigma_t^0)$ equals the interface strength for mode-I (mode-II) deformations. The slope, k_s , of straight line OA is estimated. Then

$$\sigma_i = k_s \delta_i, \quad \delta_i^0 = \frac{\sigma_i^0}{k_s}, \quad i = t, n \quad (16.a, b)$$

where k_s is called the initial interface stiffness. Thus, the delamination initiates when $\sigma_n = \sigma_n^0(\sigma_t = \sigma_t^0)$, and complete separation occurs when

$$\delta_n^f = \frac{2G_{Ic}}{\sigma_n^0}, \quad \delta_t^f = \frac{2G_{IIc}}{\sigma_t^0} \quad (17)$$

The interface stiffness k_s should be such that it does not make the system of simultaneous equations to be solved ill-conditioned and effectively prevents interpenetration between two contacting layers during compressive normal traction on the interface. One way to select the value of k_s for a beam of thickness H is to set

$$k_s = \frac{H}{\mathcal{K}} \max(\sigma_n^0, \sigma_t^0) \quad (18)$$

where \mathcal{K} is a small number.

2.1.4.2. Mixed mode deformations. For mixed-mode deformations, $\delta_n > 0$ and $\delta_t \neq 0$. We follow the approach of Ref. [8], and postulate that the delamination at a point on the interface initiates when

$$\left(\frac{\sigma_n}{\sigma_n^0}\right)^2 + \left(\frac{\sigma_t}{\sigma_t^0}\right)^2 = 1 \quad (19)$$

and complete separation occurs when

$$\left(\frac{G_I}{G_{Ic}}\right)^\beta + \left(\frac{G_{II}}{G_{IIc}}\right)^\beta = 1 \quad (20)$$

Here σ_n and σ_t are the normal and the tangential tractions on the interface under mixed-mode deformations. Similarly, G_I (G_{II}) is the strain energy release rates for mode-I (mode-II) deformations for mixed-mode loading. For composites, the exponent β is usually assigned the value 1 or 2; here we have taken it to equal 2. The exact value needs to be determined from the test data.

We define the equivalent mixed-mode relative displacement δ_e by

$$\delta_e = \sqrt{(\delta_t)^2 + (\delta_n)^2} = \frac{\delta_t}{\mu} \sqrt{1 + \mu^2} = \delta_n \sqrt{1 + \mu^2} \quad (21)$$

where $\mu \delta_n = \delta_t$, and note that $\mu = 0$ for mode-I, and $\mu \rightarrow \infty$ for mode-II deformations.

Assuming that under mixed-mode loading, the interface stiffness for the tangential and normal traction–separation modes also equals k_s , then substituting for σ_n and σ_t in terms of δ_t and δ_n into Eq. (19), the separation will initiate when

$$\left(\frac{\delta_n}{\sigma_n^0}\right)^2 + \left(\frac{\delta_t}{\sigma_t^0}\right)^2 = 1/(k_s)^2 \quad (22)$$

or equivalently,

$$\delta_e^0 = \delta_t^0 \delta_n^0 \sqrt{\frac{1 + \mu^2}{(\delta_t^0)^2 + (\mu \delta_n^0)^2}} \quad (23)$$

where δ_t^0 and δ_n^0 are given by Eq. (16.b). We assume that the mode-mixity ratio μ at a point on the interface stays constant during the delamination process, however, the value of μ can vary from point to point. The value of μ at a point is determined at the instant δ_n becomes positive. This assumption is reasonable since delamination usually occurs very quickly and any error introduced by a change in the mode mixity will be negligible.

In order to find the value δ_e^f of δ_e at complete separation, we assume that the effective traction–effective separation relation under mixed-mode loading is also triangular, i.e., similar to that for mode-I and mode-II loadings. Thus values of G_I and G_{II} at complete separation are given by

$$G_I(1 + \mu^2) = \frac{k_s \delta_e^0 \delta_e^f}{2}, \quad G_{II} = \mu^2 G_I \quad (24)$$

Substitution from Eq. (24) into Eq. (20) gives

$$\delta_e^f = \frac{2(1 + \mu^2)}{k_s \delta_e^0} \left[\left(\frac{1}{G_{Ic}}\right)^\beta + \left(\frac{\mu^2}{G_{IIc}}\right)^\beta \right]^{-1/\beta} \quad (25)$$

Because of the assumption of μ staying constant at a point, should unloading occur for $\delta_e^0 < \delta_e < \delta_e^f$, the unloading curve follows a path similar to the straight line CO in Fig. 2a for mode-I deformations.

2.2. Equations for the layerwise TSNDT

2.2.1. Displacement field

For simplicity we consider a 3-layer curved sandwich beam and denote displacements of a point in the top, the central, and the bottom layers by superscripts t , c and b , respectively. With the origin of the curvilinear coordinate axes located at the geometric centroid of the rectangular cross-section (e.g., see Fig. 3), we assume the following displacement field in the three layers of the beam.

$$u_\alpha^c(y_1, y_3, t) = \sum_{i=0}^3 (y_3)^i \omega_{\alpha i}^c(y_1, t), \quad \alpha = 1, 3, \quad |y_3| < h^c \quad (26.a)$$

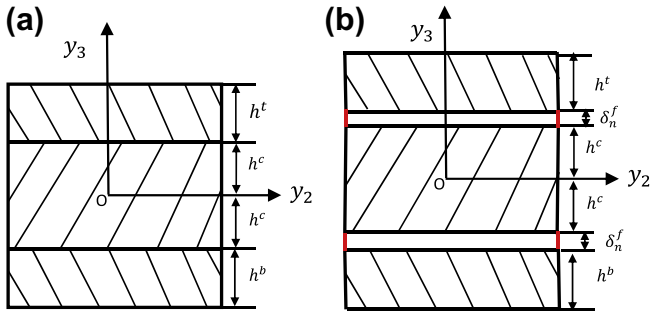


Fig. 3. Cross-section of a 3-layer beam ((a) before delamination, (b) after separation).

$$u_x^t(y_1, y_3, t) = u_x^c(y_1, h^c, t) + u_{x0}^t(y_1, t) + \sum_{i=1}^3 ((y_3)^i - (h^c)^i) u_{xi}^t(y_1, t),$$

$$\alpha = 1, 3, h^c \leq y_3 \leq h^c + h^t \quad (26.b)$$

$$u_x^b(y_1, y_3, t) = u_x^c(y_1, -h^c, t) - u_{x0}^b(y_1, t) + \sum_{i=1}^3 ((y_3)^i - (-h^c)^i) u_{xi}^b(y_1, t),$$

$$\alpha = 1, 3, -(h^b + h^c) \leq y_3 \leq -h^c \quad (26.c)$$

Here u_{i0}^c and u_{30}^c are, respectively, the axial and the transverse displacements of a point on the beam mid-surface, u_{xi}^c, u_{zi}^b and u_{xi}^t ($\alpha = 1, 3, i = 1, 2, 3$) may be interpreted as generalized axial and transverse displacements of a point, u_{x0}^t and u_{x0}^b ($\alpha = 1, 3$) equal jumps, if any, in displacements at the top and the bottom interfaces, respectively. The bottom interface is between the bottom layer and the core, and the top interface between the top layer and the core. We note that the displacement field given by Eq. (26) allows for the thickness of each layer to change, and incorporates both transverse normal and transverse shear strains. It can be written as

$$u_x(y_1, y_3, t) = \sum_{j=0}^3 (\ell_j^c(y_3) u_{xj}^c(y_1, t) + \ell_j^t(y_3) u_{xj}^t(y_1, t) + \ell_j^b(y_3) u_{xj}^b(y_1, t)),$$

$$\alpha = 1, 3 \quad (27)$$

where

$$\ell_j^c(y_3) = \begin{cases} (h^c)^j, & h^c \leq y_3 \leq h^c + h^t \\ (y_3)^j, & |y_3| < h^c \\ (-h^c)^j, & -(h^b + h^c) \leq y_3 \leq -h^c \end{cases}, \quad j = 0, 1, 2, 3 \quad (28.a)$$

$$\ell_j^t(y_3) = \begin{cases} (y_3)^j - (h^c)^j, & h^c \leq y_3 \leq h^c + h^t \\ 0, & -(h^b + h^c) \leq y_3 \leq h^c \end{cases}, \quad j = 1, 2, 3 \quad (28.b)$$

$$\ell_j^b(y_3) = \begin{cases} 0, & -h^c \leq y_3 \leq h^c + h^t \\ (y_3)^j - (-h^c)^j, & -(h^b + h^c) \leq y_3 \leq -h^c \end{cases}, \quad j = 1, 2, 3 \quad (28.c)$$

$$\ell_0^t(y_3) = \begin{cases} 1, & h^c \leq y_3 \leq h^c + h^t \\ 0, & -(h^b + h^c) \leq y_3 \leq h^c \end{cases},$$

$$\ell_0^b = \begin{cases} 0, & -h^c \leq y_3 \leq h^c + h^t \\ -1, & -(h^b + h^c) \leq y_3 \leq -h^c \end{cases} \quad (28.d)$$

We can thus rewrite Eq. (26) as

$$u_x(y_1, y_3, t) = \sum_{j=1}^{12} L_j(y_3) u_{xj}(y_1, t), \quad \alpha = 1, 3 \quad (29)$$

where

$$L_j = \begin{cases} \ell_{j-1}^c, & j = 1, 2, 3, 4 \\ \ell_{j-5}^t, & j = 5, 6, 7, 8 \\ \ell_{j-9}^b, & j = 9, 10, 11, 12 \end{cases}; \quad u_{xj} = \begin{cases} u_{x(j-1)}^c, & j = 1, 2, 3, 4 \\ u_{x(j-5)}^t, & j = 5, 6, 7, 8 \\ u_{x(j-9)}^b, & j = 9, 10, 11, 12 \end{cases} \quad (30)$$

Displacements δ_n and δ_t at the interface between the top layer and the core appearing in Eq. (16.a) are related to the displacement field $u_x(y_1, y_3, t)$ by substituting from Eq. (29) into Eq. (9). Thus for the top layer

$$\delta_t = \mathbb{R}_{1\alpha} u_{x0}^t, \delta_n = \mathbb{R}_{3\alpha} u_{x0}^t, \alpha = 1, 3, \text{ summed on } \alpha \quad (31)$$

2.2.2. Governing equations

We multiply both sides of Eq. (8a,b) with $L_j(y_3)$ ($j = 1, 2, \dots, 12$), integrate both sides of the resulting equation over the beam thickness (i.e., with respect to y_3), and obtain

$$\int_{-h^c-h^b}^{h^c+h^t} L_j(y_3) \rho_0 \ddot{u}_1 H_1 dy_3 = \int_{-h^c-h^b}^{h^c+h^t} L_j(y_3) \left[\frac{\partial T_{11}}{\partial y_1} + \frac{\partial (H_1 T_{13})}{\partial y_3} + \frac{1}{R} T_{31} + H_1 f_1 \right] dy_3$$

$$\int_{-h^c-h^b}^{h^c+h^t} L_j(y_3) \rho_0 \ddot{u}_3 H_1 dy_3 = \int_{-h^c-h^b}^{h^c+h^t} L_j(y_3) \left[\frac{\partial T_{31}}{\partial y_1} + \frac{\partial (H_1 T_{33})}{\partial y_3} - \frac{1}{R} T_{11} + H_1 f_3 \right] dy_3 \quad (32)$$

Substituting from Eq. (30) into Eq. (32) and integrating by parts the 2nd term in brackets in the integrand on the right-hand side of Eq. (32) with respect to y_3 , we get

$$A_{ji} \ddot{u}_{1i} = \frac{\partial M_{11}^j}{\partial y_1} - \bar{M}_{13}^j + \frac{1}{R} M_{31}^j + \bar{f}_1^j + B_{13}^j + C_{13}^j, \quad i, j = 1, 2, \dots, 12 \quad (33.a)$$

$$A_{ji} \ddot{u}_{3i} = \frac{\partial M_{31}^j}{\partial y_1} - \bar{M}_{33}^j - \frac{1}{R} M_{11}^j + \bar{f}_3^j + B_{33}^j + C_{33}^j, \quad i, j = 1, 2, \dots, 12 \quad (33.b)$$

where

$$M_{mn}^j(y_1, t) = \int_{-h^c-h^b}^{h^c+h^t} L_j(y_3) T_{mn} \mathcal{H}_{(n)} dy_3, \quad \mathcal{H}_{(1)} = 1, \mathcal{H}_{(3)} = H_1, m, n = 1, 3 \quad (34.a)$$

$$\bar{M}_{mn}^j(y_1, t) = \int_{-h^c-h^b}^{h^c+h^t} \frac{dL_j(y_3)}{dy_3} T_{mn} \mathcal{H}_{(n)} dy_3, \quad \mathcal{H}_{(1)} = 1, \mathcal{H}_{(3)} = H_1, m, n = 1, 3 \quad (34.b)$$

$$B_{13}^j(y_1, t) = L_j(h^c + h^t) H_1 T_{13}(h^c + h^t, t) - L_j(-h^c - h^b) H_1 T_{13}(-h^c - h^b, t) \quad (34.c)$$

$$B_{33}^j(y_1, t) = L_j(h^c + h^t) H_1 T_{33}(h^c + h^t, t) - L_j(-h^c - h^b) H_1 T_{33}(-h^c - h^b, t) \quad (34.d)$$

$$C_{13}^j(y_1, t) = (L_j(h^c) - L_j(h^c)) H_1 \bar{f}_1^c(h^c) + (L_j(-h^c) - L_j(-h^c)) H_1 \bar{f}_1^c(-h^c) \quad (34.e)$$

$$C_{33}^j(y_1, t) = (L_j(h^c) - L_j(h^c)) H_1 \bar{f}_3^c(h^c) + (L_j(-h^c) - L_j(-h^c)) H_1 \bar{f}_3^c(-h^c) \quad (34.f)$$

$$\bar{f}_z^j(y_1, t) = \int_{-h^c-h^b}^{h^c+h^t} L_j(y_3) f_z H_1 dy_3, \quad \alpha = 1, 3 \quad (34.g)$$

$$A_{ji}(y_1, t) = \int_{-h^c-h^b}^{h^c+h^t} L_j(y_3) L_i(y_3) \rho_0 H_1 dy_3 \quad (34.h)$$

The quantity M_{mn}^j equals j th order moment of the stress T_{mn} about the y_2 -axis. Quantities B_{13}^j and B_{33}^j equal, respectively, j th order moments about the y_2 -axis of the tangential surface traction T_{13} and the normal surface traction T_{33} applied on the top and the bottom surfaces of the beam, and quantities C_{13}^j and C_{33}^j equal, respectively, j th order moments about the y_2 -axis of the tangential surface traction $\bar{f}_1^{c\pm}$ and the normal surface traction $\bar{f}_3^{c\pm}$ acting on the cohesive interface of the beam. Similarly, \bar{f}_z^j equals j th order moment of the body force f_z about the y_2 -axis, and A_{ji} is the inertia tensor associated with the generalized displacements u_{1i} and u_{3i} . The quantity $L_j(-h^{c\pm})$ equals the value of the function $L_j(y_3)$ at the interface between the core and the bottom layer, and $h^{c\pm}$ equals the value of y_3 on Γ_{\pm}^c .

Assuming that we have cohesive surfaces at the two interfaces between the core and the two surrounding layers, $\bar{f}_1^{c-}(h^c)$ and $\bar{f}_3^{c-}(h^c)$ represent, respectively, the tangential and the normal tractions on the cohesive interface between the top layer and the core. Similarly, $\bar{f}_1^{c+}(-h^c)$ and $\bar{f}_3^{c+}(-h^c)$ represent, respectively, the tangential and the normal tractions on the cohesive interface between the bottom layer and the core. These tractions are measured per unit area in the reference configuration, and are related to the cohesive stresses σ_n and σ_t given by Eq. (8.f). Substituting for $\bar{f}_1^{c\pm}$ and $\bar{f}_3^{c\pm}$ from the traction–separation relations similar to those in Eq. (16.a) into Eqs. (34.e) and (34.f) we express C_{13}^j and C_{33}^j in terms of displacements δ_n and δ_t , or equivalently in terms of u_{x0}^t and u_{x0}^b because of Eq. (31).

Eq. (33a, b) governing deformations of the beam incorporates surface tractions acting on the top and the bottom surfaces of the beam. Substitution for T_{mn} in terms of displacement gradients from Eqs. (12) and (14) into Eq. (34) gives expressions for moments M_{mn}^j, \bar{M}_{mn}^j and C_{mn}^j in terms of displacements. Substituting these in Eq. (33), we obtain nonlinear coupled partial differential equations (PDEs) for u_{1j} and u_{3j} for the TSNDT. These 24 PDEs involve second-order derivatives of u_{1j} and u_{3j} with respect to y_1 and time t , and are to be solved under pertinent initial and boundary conditions.

We consider the case of zero initial displacements and velocities. Thus

$$u_{\alpha j}^0(y_1, t) = 0, \dot{u}_{\alpha j}^0(y_1, t) = 0 \quad \alpha = 1, 3, \quad j = 1, 2, \dots, 12 \quad (35.a, b)$$

Boundary conditions at a clamped, simply supported and traction free edge, say $y_1 = 0$, respectively, are

$$u_{\alpha j}(0, t) = 0, \alpha = 1, 3, j = 1, 2, \dots, 12 \quad (36.a)$$

$$u_{3j}(0, t) = 0, M_{11}^j(0, t) = 0, \quad (36.b)$$

$$M_{11}^j(0, t) = 0, M_{31}^j(0, t) = 0 \quad (36.c)$$

3. Finite element formulation of the problem

3.1. Weak formulation

Let Θ_1^j and Θ_3^j be smooth functions of $y_1 \in [0, L]$. We take the inner product of both sides of Eqs. (33.a) and (33.b) with Θ_1^j and Θ_3^j , respectively, integrate the resulting equations with respect to y_1 on $[0, L]$, and then integrate by parts the terms involving $\frac{\partial M_{11}^j}{\partial y_1}$ and $\frac{\partial M_{31}^j}{\partial y_1}$ to arrive at the following equations:

$$\int_0^L \Theta_1^j (A_{ji} \ddot{u}_{1i}) dy_1 = \int_0^L \left(-\frac{\partial \Theta_1^j}{\partial y_1} M_{11}^j + \Theta_1^j \left(\frac{1}{R} M_{31}^j + \bar{f}_1^j + B_{13}^j + C_{13}^j - \bar{M}_{13}^j \right) \right) dy_1 + B_{11} \\ \int_0^L \Theta_3^j (A_{ji} \ddot{u}_{3i}) dy_1 = \int_0^L \left(-\frac{\partial \Theta_3^j}{\partial y_1} M_{31}^j + \Theta_3^j \left(\bar{f}_3^j + B_{33}^j + C_{33}^j - \bar{M}_{33}^j - \frac{1}{R} M_{11}^j \right) \right) dy_1 + B_{31} \quad (37)$$

where

$$B_{11} = \Theta_1^j(L) M_{11}^j(L) - \Theta_1^j(0) M_{11}^j(0), \\ B_{31} = \Theta_3^j(L) M_{31}^j(L) - \Theta_3^j(0) M_{31}^j(0) \quad (38)$$

Here indices $i, j = 1, 2, \dots, 12$. If one thinks of Θ_1^j and Θ_3^j as virtual displacements that vanish at boundary points where displacements are prescribed, then Eq. (37) states the principle of virtual work. Alternatively, Eq. (37) expresses a weak formulation of the problem since it involves first-order derivatives of u_1 and u_3 with respect to y_1 whereas the PDEs (33) have second-order derivatives of u_1 and u_3 with respect to y_1 . Since T_{11}, T_{13}, T_{31} and T_{33} are nonlinear functions of displacement gradients, Eq. (37) is nonlinear in u_1 and u_3 .

3.2. Derivation of ordinary differential equations

We discretize the curve along the y_1 -axis into one-dimensional finite elements (FEs) of not necessarily the same length. Let there be N nodes on this curve and $\Psi_1(y_1), \Psi_2(y_1), \dots, \Psi_N(y_1)$ be the FE basis functions. We write

$$u_{\alpha j}(y_1, t) = \sum_{i=1}^N \Psi_i(y_1) \tilde{d}_{\alpha j i}(t), \quad j = 1, 2, \dots, 12; \quad \alpha = 1, 3 \quad (39)$$

Thus we have 24 N unknown functions $\tilde{d}_{\alpha j i}(t), \alpha = 1, 3; i = 1, 2, \dots, N; j = 1, 2, \dots, 12$. We write these as the 24 N-dimensional vector $\mathbf{d}(t)$, and the displacement field $u_{\alpha j}(y_1, t)$ as 24-dimensional vector $\tilde{\mathbf{u}}(y_1, t)$. These can be written as

$$\{\tilde{\mathbf{u}}(y_1, t)\} = [\emptyset(y_1)] \{\mathbf{d}(t)\} \\ \{\tilde{\mathbf{u}}(y_1, t)\} = \{u_{1j} \quad u_{3j}\}^T, \quad j = 1, 2, \dots, 12 \quad (40)$$

where $[\emptyset]$ is 24×24 N matrix and $\{\mathbf{d}\}$ is 24 N \times 1 matrix. In index notation, Eq. (40) becomes

$$\tilde{u}_i(y_1, t) = \emptyset_{ij}(y_1) d_j(t), \quad i = 1, 2, \dots, 24; \quad j = 1, 2, \dots, 24 \quad (41)$$

We can also write the displacement fields $u_1(y_1, y_3, t)$ and $u_3(y_1, y_3, t)$ as

$$\begin{Bmatrix} u_1(y_1, y_3, t) \\ u_3(y_1, y_3, t) \end{Bmatrix} = [\phi(y_3)] [\emptyset(y_1)] \{\mathbf{d}(t)\} = [\Phi(y_1, y_3)] \{\mathbf{d}(t)\} \quad (42)$$

where $[\phi(y_3)] = \begin{bmatrix} L(y_3) & 0 \\ 0 & L(y_3) \end{bmatrix}$ is 2×24 matrix, $[\emptyset(y_1)]$ is 24×24 N matrix and $[\Phi]$ is 2×24 N matrix.

We use the Galerkin formulation and take the same basis functions for the test functions Θ_1^j, Θ_3^j as those for the trial solutions u_{1j}, u_{3j} ; e.g., see Eq. (39). That is

$$\Theta_{\alpha}^j(y_1) = \sum_{i=1}^N \Psi_i(y_1) c_{\alpha i}^j, \quad \alpha = 1, 3; \quad j = 1, 2, \dots, 12 \quad (43)$$

where $c_{\alpha i}^j$ are 24 N constants.

Substitution from Eqs. (40) and (43) into Eq. (37) and requiring that the resulting equations hold for all values of constants $c_{\alpha i}^j$ gives the following set of coupled nonlinear ordinary differential equations (ODEs).

$$\mathbf{M} \ddot{\mathbf{d}} = \mathbf{F}^{\text{ext}} + \mathbf{F}^c - \mathbf{F}^{\text{int}}(\mathbf{d}), \quad (44)$$

where

$$\mathbf{M} = \int_0^L [\emptyset(y_1)]^T [\bar{\mathbf{A}}] [\emptyset(y_1)] dy_1, \quad [\bar{\mathbf{A}}] = \begin{bmatrix} \mathbf{A} & \mathbf{0} \\ \mathbf{0} & \mathbf{A} \end{bmatrix} \quad (45.a)$$

$$\mathbf{F}^{\text{ext}} = \int_0^L [\emptyset(y_1)]^T \begin{Bmatrix} \text{vec}(\bar{f}_1^j + B_{13}^j) \\ \text{vec}(\bar{f}_3^j + B_{33}^j) \end{Bmatrix} dy_1 + [\emptyset(L)]^T \begin{Bmatrix} \text{vec}(M_{11}^j(L)) \\ \text{vec}(M_{31}^j(L)) \end{Bmatrix} \\ - [\emptyset(0)]^T \begin{Bmatrix} \text{vec}(M_{11}^j(0)) \\ \text{vec}(M_{31}^j(0)) \end{Bmatrix} \quad (45.b)$$

$$\mathbf{F}^c = \int_0^L [\emptyset(y_1)]^T \begin{Bmatrix} \text{vec}(C_{13}^j) \\ \text{vec}(C_{33}^j) \end{Bmatrix} dy_1 \quad (45.c)$$

$$\mathbf{F}^{\text{int}} = \int_0^L [BL]^T \left\{ \text{vec}(M_{11}^j) \quad \text{vec}(M_{31}^j) \quad \text{vec}(\bar{M}_{13}^j - \frac{1}{R} M_{31}^j) \quad \text{vec}(\bar{M}_{33}^j + \frac{1}{R} M_{11}^j) \right\}^T dy_1 \quad (45.d)$$

$$[BL1] = \begin{bmatrix} \text{diag}\left(\frac{\partial}{\partial y_1}\right) & 0 \\ 0 & \text{diag}\left(\frac{\partial}{\partial y_1}\right) \\ \text{diag}(1) & 0 \\ 0 & \text{diag}(1) \end{bmatrix} [\emptyset(y_1)], \quad (45.e)$$

$$\text{diag}(f) = \text{diagonal}\{f^1 \ f^2 \ \dots \ f^{12}\}, (12 \text{ terms})$$

$$\text{diag}(f^j) = \text{diagonal}(f^1 \ f^2 \ \dots \ f^{12}), \text{vec}(f^j) = \{f^1 \ f^2 \ \dots \ f^{12}\} \quad (45.f)$$

Here $\mathbf{M} = \mathbf{M}^T$ is the consistent mass matrix, the 12 x 12 matrix A is given by Eq. (34.h), \mathbf{F}^{ext} represents the generalized 24 N-dimensional nodal force (\mathbf{F}^{ext} is $24 N \times 1$ matrix) equivalent to the externally applied surface tractions on boundaries and the body force (e.g., gravity). The 24 N-dimensional vector \mathbf{F}^{int} represents forces due to internal stresses, and is a nonlinear function of the generalized nodal displacement \mathbf{d} since stresses T_{11} , T_{13} , T_{31} and T_{33} are nonlinear functions of u_1 and u_3 . \mathbf{F}^c represents the force vector due to tractions applied on the cohesive interface. The weak formulation involves only first-order derivatives of generalized displacements. Thus C^0 basis functions can be used to numerically analyze the problem. For example, for plates made of linear elastic materials, Qian et al. [16] and Xiao et al. [17] have used, respectively, basis functions derived by the moving least squares approximation and radial basis functions in meshless methods to study transient deformations of thick plates using K^{th} order shear and normal deformable plate theory. Batra and Aimmanee [29] have used the same plate theory and the FE basis functions to analyze free vibrations of a plate. Here we consider material and geometric nonlinearities and use the TSNDT.

Integrals in Eq. (45) are numerically evaluated by using three Gauss integration points in each FE along the y_1 -axis except in Eqs. (45.c) and (45.d) where we use only one Gauss point in a FE along the y_1 -axis. Recall that jump displacements at nodes on the cohesive interface are included in \mathbf{d} .

If the edge, $y_1 = 0$, where node 1 is located, of the beam is clamped, simply supported or free, boundary conditions there are, respectively, given by Eqs. (46), (47) and (48).

$$\tilde{d}_{\alpha 1j}(t) = 0, \quad j = 1, 2, \dots, 12; \quad \alpha = 1, 3; \quad (46)$$

$$\tilde{d}_{31j}(t) = 0, \quad M_{11}^j(0, t) = 0, \quad j = 1, 2, \dots, 12; \quad (47.a, b)$$

$$M_{11}^j(0, t) = 0, \quad M_{31}^j(0, t) = 0, \quad j = 1, 2, \dots, 12. \quad (48)$$

3.3. Solution of nonlinear ODEs

We use the conditionally stable central-difference method to integrate the coupled nonlinear ODEs (44). That is, with the notation

$$\mathbf{d}^{n+1} = \mathbf{d}(t_{n+1}), \quad (49)$$

we have

$$\mathbf{d}^{n+1} = \mathbf{d}^n + \Delta t \dot{\mathbf{d}}^n + \frac{\Delta t^2}{2} \ddot{\mathbf{d}}^n, \quad (50.a)$$

$$\ddot{\mathbf{d}}^{n+1} = \mathbf{M}^{-1} [\mathbf{F}^{\text{ext}}(t_{n+1}) + \mathbf{F}^c(\mathbf{d}^{n+1}) - \mathbf{F}^{\text{int}}(\mathbf{d}^{n+1})], \quad (50.b)$$

$$\dot{\mathbf{d}}^{n+1} = \dot{\mathbf{d}}^n + \frac{\Delta t}{2} (\ddot{\mathbf{d}}^{n+1} + \ddot{\mathbf{d}}^n). \quad (50.c)$$

The critical time step size to compute a stable solution is determined by finding the maximum frequency, ω_{max} , of free vibrations and taking $\Delta t \leq \Delta t_{\text{crit}}$, $\Delta t_{\text{crit}} = 2/\omega_{\text{max}}$. Ideally, ω_{max} should be found after every time step since frequencies of a structure change as it is

deformed. The accuracy of the solution can be improved by taking $\Delta t \ll \Delta t_{\text{crit}}$ but at the cost of increasing the computational time.

Results presented in Section 4 have been computed with a consistent mass matrix and $\Delta t = 0.9 \Delta t_{\text{crit}}$ for a linear problem but $\Delta t = 0.5 \Delta t_{\text{crit}}$ for a nonlinear problem. For the nonlinear problems, ω_{max} found from analyzing frequencies of the undeformed beam is used to ascertain Δt_{crit} .

For a static problem, the nonlinear algebraic Eq. (44) is solved for \mathbf{d} by the modified Newton–Raphson method. That is, we iteratively solve

$$\mathbf{F}^{\text{int}}(\mathbf{d}) - \mathbf{F}^c(\mathbf{d}) = \mathbf{F}^{\text{ext}} \quad (51)$$

by first writing it as

$$\mathbf{K} \Delta \mathbf{d} = -(\mathbf{F}^{\text{int}}(\bar{\mathbf{d}}) - \mathbf{F}^c(\bar{\mathbf{d}}) - \mathbf{F}^{\text{ext}}), \quad \mathbf{K} = \left. \frac{\partial(\mathbf{F}^{\text{int}} - \mathbf{F}^c)}{\partial \mathbf{d}} \right|_{\mathbf{d}=\bar{\mathbf{d}}}, \quad \mathbf{d} = \bar{\mathbf{d}} + \Delta \mathbf{d} \quad (52)$$

The iterative process is terminated when the norm of the residual load vector, $\bar{\mathbf{R}}$, defined by

$$\mathbf{R} = \mathbf{F}^{\text{int}}(\mathbf{d}) - \mathbf{F}^c(\mathbf{d}) - \mathbf{F}^{\text{ext}}, \quad \bar{\mathbf{R}} = \max(|\mathbf{R}|)N/\text{Sum}(|\mathbf{F}^{\text{ext}}|) \quad (53)$$

is less than 0.05%. Recall that N equals the number of nodes. For every load step the stiffness matrix \mathbf{K} is evaluated only once.

4. Example problems

We use the more common notation and replace y_1 and y_3 by x and z , respectively. Subscripts 1, 2 and 3 represent directions along the x -, the y - and the z -axes, respectively. When analyzing problems without considering geometric nonlinearities, we omit all nonlinear terms in expressions for the strain components and rotation of the cohesive interface, and note that differences among the three stress tensors, namely, the 1st and the 2nd Piola–Kirchhoff and the Cauchy stress tensors are negligible.

4.1. Delamination in quasistatic deformations of a pre-delaminated linear elastic beam

4.1.1. Mode-I deformations under monotonically increasing load

We study the initiation and propagation of delamination in mode-I deformations of a double cantilever beam (DCB) and compare computed results with the numerical results of Ref. [7], and experimental findings of Ref. [18]. We note that the beam undergoes mode-I deformations when $-\Delta_3^b = \Delta_3^t = \Delta_3$ in Fig. 4a. In order to use the 3-layer formulation described above, we divide the bottom layer of the DCB into two layers of equal thickness, and introduce the cohesive interface only between the upper two layers. The thickness of the top, the middle and the bottom layers of the beam are given by $h^t = h$, $2h^c = \frac{h}{2}$ and $h^b = \frac{h}{2}$, respectively. Thus the z -coordinate of points on the bottom and the top surfaces of the DCB equal $-0.75h$ and $1.25h$, respectively.

Boundary conditions at the clamped edge $x = 0$ are given by Eq. (46). We enforce boundary conditions $-\Delta_3^b = \Delta_3^t = \Delta_3$ at $x = \mathcal{L}$ by applying

$$\epsilon_{30}^c(\mathcal{L}) = -\Delta_3, \quad \epsilon_{30}^t(\mathcal{L}) = 2\Delta_3, \quad \epsilon_{30}^b(\mathcal{L}) = 0 \quad (54.a)$$

$$\epsilon_{3i}^c(\mathcal{L}) = \epsilon_{3i}^b(\mathcal{L}) = \epsilon_{3i}^t(\mathcal{L}) = 0, \quad i = 1, 2, 3 \quad (54.b)$$

$$M_{11}^j(\mathcal{L}) = 0, \quad j = 1, 2, \dots, 12 \quad (54.c)$$

The displacement Δ_3 is applied in increments of 0.01 mm. Forces P_3^t and P_3^b are evaluated by integrating computed values of $T_{31}(\mathcal{L}) = \sigma_{xz}(\mathcal{L})$ for the upper and the lower layers of the DCB, respectively, and multiplying the result with the beam width B . For this problem, $\delta_n(y_1) = \epsilon_{30}^t(y_1)$.

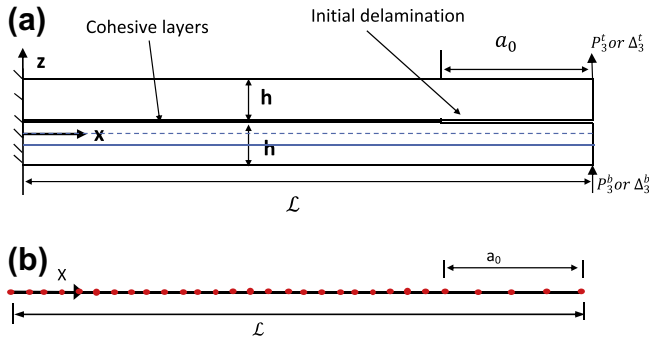


Fig. 4. (a) Sketch of a pre-delaminated beam with either point loads or transverse displacements applied at the ends, (b) FE mesh on the reference surface of the beam.

Material and geometric parameters are assigned following values taken from [7].

$$\begin{aligned}
 E_1 &= 130 \text{ GPa}, G_{13} = 2.0 \text{ GPa}, G_{lc} = 275 \text{ Jm}^{-2}, \sigma_n^0 = 60 \text{ MPa} \\
 E_2 &= E_3 = 7.5 \text{ GPa}, \nu_{12} = \nu_{13} = 0.3, \nu_{23} = 0.3 \\
 L &= 100 \text{ mm}, a_0 = 45 \text{ mm}, h = 2 \text{ mm}, B = 15 \text{ mm}
 \end{aligned}$$

(55)

Here a_0 equals the initial delaminated length and $2h$ the total thickness of the DCB. The FE mesh shown in Fig. 4b has 2-node elements with element size in the in-tact region equal to half of that in the initial delaminated region. The experimental value of the tensile strength σ_n^0 was not provided in [18] and was assumed to be 60 MPa in [7]. Here results have been computed for two values, 30 and 60 MPa, of σ_n^0 that are representative of the matrix strength.

In the delaminated region, integrals in Eq. (31) over the thickness are written as the sum of two integrals, one from $-(h^c + h^b)$ to h^c and the other from h^c to $(h^c + h^t)$ with the interface between the core and the top layer regarded as traction free. Thus the effective stiffness of the delaminated beam is less than that of the intact beam.

The computed load vs. edge displacement curves for $\sigma_n^0 = 30$ and 60 MPa, two FE meshes and two values of the initial stiffness k_s of the cohesive traction–separation relation are compared in Fig. 5 with those reported in Refs. [7,18]. Furthermore, in Fig. 6, the presently computed load vs. the delaminated length curve is compared with that given in [7]. It is clear from these plots that the present work accurately analyzes mode-I delamination of a DCB specimen. Effects of the initial stiffness ($\mathcal{K} = 10^{-8}$ or 10^{-9} in Eq. (18)) in the cohesive traction separation relation and of the interfacial strength (30 or 60 MPa) on the computed load–displacement curves are insignificant.

The variations with the edge displacement of the strain energy W_e stored in the DCB, the work done by external forces and the energy dissipated during delamination are exhibited in Fig. 7. The energy W_e is evaluated by integrating the elastic energy density W (cf. Eq. (10)) over the beam domain, the work W_p of external forces equals $\int P_3^t d\Delta_3^t + \int P_3^b d\Delta_3^b$, and the energy W_d dissipated during delamination equals $\int_{r_c} B G_{lc} dy_1$. It is clear that the delamination begins to grow when the edge displacement and the load equal about 1.5 mm and 45 N, respectively. The energy dissipated during delamination is comparable to the elastic energy stored in the beam. The maximum percentage difference $100(W_p - W_e - W_d)/W_p$ equals 0.6% signifying that the balance of energy is well satisfied.

The line PQR perpendicular to the centroidal axis at $x = 40$ mm in the reference configuration is deformed into line segments P'Q' and Q''R' shown in Fig. 8. Thus abutting particles of the lower and the upper layers that occupied the place Q in the reference configuration are deformed into places Q'' and Q' respectively, and Q'Q''

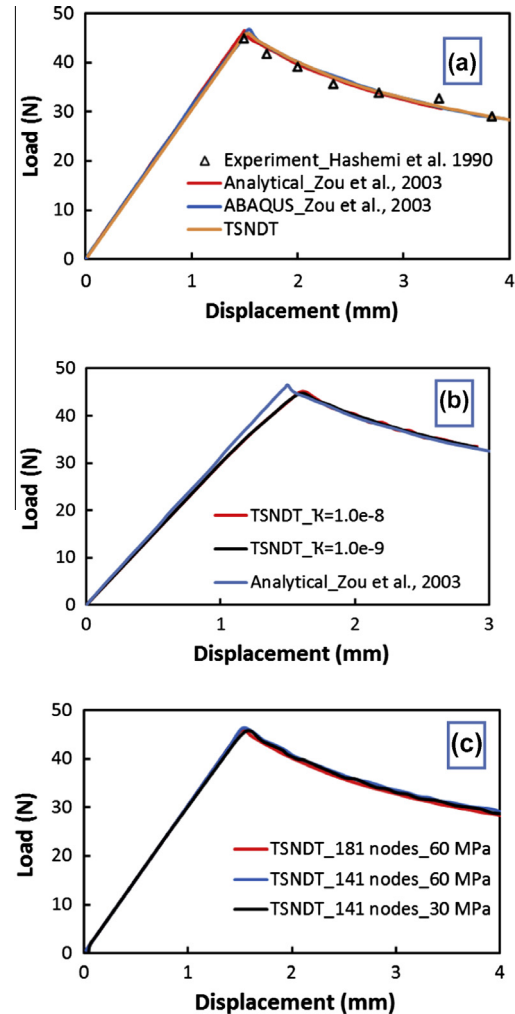


Fig. 5. For quasistatic mode-I deformations of the DCB specimen, comparison of the presently computed load (P_3^t)-end displacement (Δ_3^t) curves with numerical results of Ref. [7] and experimental findings of Ref. [18]. (a) and (b) $\sigma_n^0 = 60$ MPa (181 nodes), (c) load vs. displacement curves for two values, 60 and 30 MPa, of the cohesive strength σ_n^0 .

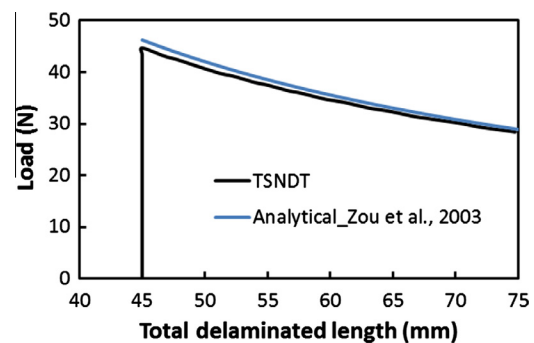


Fig. 6. Load P_3^t vs. delaminated length, $\sigma_n^0 = 60$ MPa (181 nodes).

equals the jump $\delta_n(x) = \epsilon_{30}^t(x)$ at $x = 40$ mm. It is also evident that segments PQ and QR are rotated, respectively, into lines P'Q' and Q''R' that have slopes of opposite signs.

4.1.2. Mode-I deformations under cyclic load

We now study mode-I deformations of the DCB analyzed in subsection 4.1.1 during loading, unloading and reloading. We use increments of 0.01 mm to first increase Δ_3 at the edge $x = L$ from

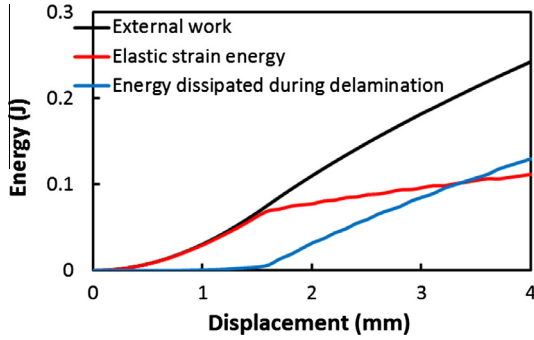


Fig. 7. Variation with the edge displacement of the work done by external forces, strain energy stored in the beam and energy dissipated during delamination, $\sigma_n^0 = 60$ MPa (181 nodes).

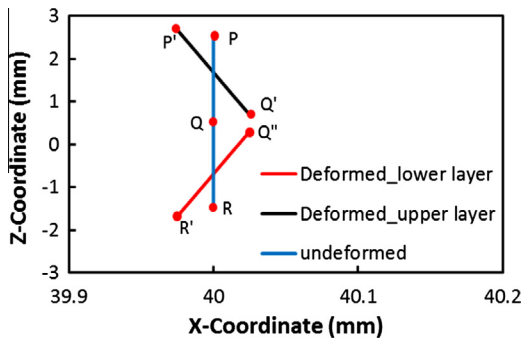


Fig. 8. Deformed configurations of a line initially perpendicular to the centroidal axis at $x = 40$ mm when $\Delta_3 = 3.42$ mm.

0 to 2 mm, then decrease Δ_3 to zero, and finally increase Δ_3 to 3 mm. Variations with Δ_3 of the load and different components of energy are shown in Figs. 9 and 10, respectively. The load vs. displacement curve in Fig. 9 is given by OAB during initial loading, by BO during unloading to zero value of Δ_3 , and by OBC during subsequent reloading. From results depicted in Fig. 10 we see that the energy dissipated because of delamination during unloading is zero (e.g., the curve AE in Fig. 10) and no additional energy is dissipated till the specimen has been reloaded to the state (corresponding to point A in Fig. 10) from which it was unloaded. The work done by external force follows the path OC during initial loading and CDE during unloading. It is clear that during the full cycle of loading and unloading the net work done by external forces corresponding to point E in Fig. 10 equals the energy used to damage the cohesive layer of the DCB as evidenced by a decrease in its stiffness from the slope of line OA to the slope of line OB in Fig. 9. The area of triangle OAB equals the energy corresponding to point E in Fig. 10. The strain energy of deformation follows the path OFB during initial loading and the path BO during unloading. Thus all of the energy stored in the body is recovered during unloading as should be the case for an elastic problem. The curve BO is essentially parallel to the curve CDE with the vertical distance between the two curves equaling the energy corresponding to point A or that used to damage the cohesive layer. These results suggest that the present software correctly predicts deformations during loading, unloading and reloading process.

4.1.3. Mode-II deformations under monotonically increasing load

When the beam shown in Fig. 4a is deformed by prescribing displacements $\Delta_3^b = \Delta_3^t = \Delta_3$ and the beam undergoes mode-II deformations, the beam is called the End Load Split (ELS) specimen [19]. We assume that the beam is made of an isotropic material

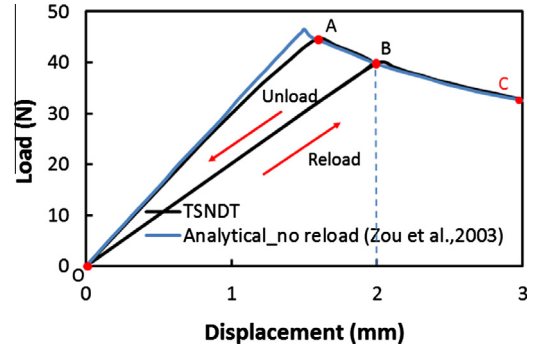


Fig. 9. For $\sigma_n^0 = 60$ MPa and quasistatic mode-I deformations of the DCB, load (P_3^t)-edge displacement (Δ_3^t) curves during loading, unloading and reloading. The analytical results are obtained by using equations given in [7], and numerical results were computed using 181 nodes.

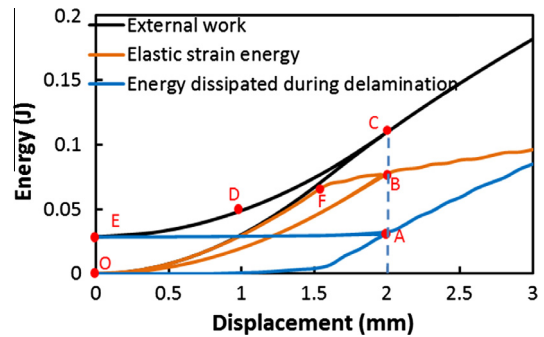


Fig. 10. Variation with the edge displacement of the work done by external forces, strain energy stored in the beam and energy dissipated during delamination.

with following values of material and geometric parameters taken from [20,21].

$$E = 150 \text{ GPa}, \nu = 0.25, G_{IIc} = 1.45 \text{ kJ m}^{-2}, \sigma_t^0 = 80 \text{ MPa}$$

$$\mathcal{L} = 100 \text{ mm}, a_0 = 50 \text{ mm}, 2h = 3 \text{ mm}, B = 10 \text{ mm} \quad (56)$$

Presently computed numerical results are compared with the analytical results based on the LEFM approach reported in [20] and numerical results given in [21] that were computed with a user defined cohesive element subroutine implemented in ABAQUS.

Boundary conditions $\Delta_3^b = \Delta_3^t = \Delta_3$ for mode-II deformations of the beam shown in Fig. 4a are satisfied by setting

$$u_{30}^c(\mathcal{L}) = \Delta_3, u_{30}^t(\mathcal{L}) = 0, u_{30}^b(\mathcal{L}) = 0 \quad (57.a)$$

$$u_{3i}^c(\mathcal{L}) = u_{3i}^b(\mathcal{L}) = u_{3i}^t(\mathcal{L}) = 0, M_{11}^i(\mathcal{L}) = 0, j = 1, 2, \dots, 12, i = 1, 2, 3 \quad (57.b)$$

The displacement Δ_3 is applied in increments of 0.05 mm and values of $P_3 = P_3^t + P_3^b$ are found by integrating over the thickness computed values of $T_{31}(\mathcal{L}) = \sigma_{xz}(\mathcal{L})$ for the upper and the lower layers of the beam, and multiplying the result with the beam width B . The presently computed load P_3 -displacement Δ_3 curves for mode-II delamination exhibited in Fig. 11a are close to those reported in Refs. [20,21]. The load vs. displacement curves in Fig. 11b for two values, 60 and 80 MPa, of σ_t^0 , and two different FE meshes, are essentially identical to each other signifying negligible effect of the precise value of σ_t^0 used to compute results, and whether 81 or 121 nodes are used to discretize the length \mathcal{L} of the beam. The beam begins to delaminate when $\Delta_3 = 14.8$ mm as signified by a drop in the load in Fig. 11a. The presently computed peak load differs from that reported in Refs. [20,21] by 2.7% and 1.8%, respectively. With an increase in the delamination length the load continues to drop till $\Delta_3 = 23$ mm at which instant the load begins

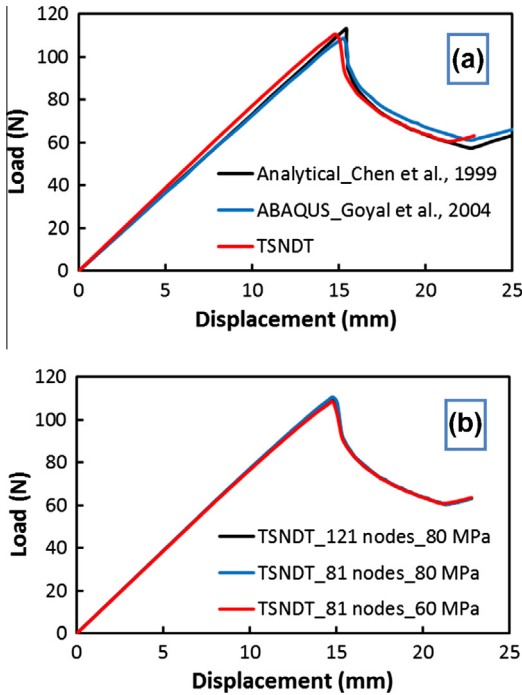


Fig. 11. Load (P_3)-edge displacement (Δ_3) curves for mode-II deformations using 81 nodes. (a) Comparison of present results with those of [20,21] (121 nodes), (b) load vs. displacement curves for two values, 60 and 80 MPa, of the cohesive strength σ_t^0 , and two FE meshes having 81 and 121 nodes.

to increase because the delamination has propagated to the end of the beam as depicted in Fig. 12.

The delaminated lengths for $\Delta_3 = 14.3$ mm and 17.5 mm are 50 mm and 77 mm, respectively. That is, the interface between the lower surface of the top beam and the upper surface of the bottom beam at $x = 40$ mm is not delaminated when $\Delta_3 = 14.3$ mm but is delaminated when $\Delta_3 = 17.5$ mm. We have plotted in Figs. 13 and 14, respectively, the variation at $x = 40$ mm of σ_{xz} and σ_{xx} for $\Delta_3 = 14.3$ mm and 17.5 mm. It is clear that σ_{xz} and σ_{xx} are continuous across the interface before delamination. The axial stress σ_{xx} continuously varies from +422 MPa to -422 MPa from the bottom to the top surface. Subsequent to delamination, the two layers deform independently and σ_{xz} equals zero on the interface since the contacting smooth delaminated surfaces have zero tangential tractions. The through-the-thickness variations of σ_{xx} in the two layers of the beam are identical to each other since they have the same bending stiffness and curvature.

The deformed configurations of line PQR initially perpendicular to the centroidal axis at $x = 40$ mm when $\Delta_3 = 17.5$ mm are shown in Fig. 15. Segments PQ and QR of line PQR are deformed into P'Q' and Q'R' that are parallel to each other. The distance Q'Q' equals the jump $\delta_t(x) = \omega_{t0}^t(x)$ at $x = 40$ mm.

4.1.4. Mixed-mode deformations under monotonically increasing load

Following the terminology of [22], we call the fracture test shown in Fig. 4a when $\Delta_3^b = -\Delta_3, P_3^t = 0$ and the beam undergoes mixed mode deformations the Fixed Ratio Mixed Mode (FRMM) test. We use following values of the material and the geometric parameters taken from Ref. [21].

$$\begin{aligned}
 E_1 &= 150 \text{ GPa}, G_{13} = 6.0 \text{ GPa}, G_{Ic} = 352 \text{ Jm}^{-2}, G_{IIc} = 1.45k \text{ Jm}^{-2} \\
 E_2 = E_3 &= 11.0 \text{ GPa}, \nu_{12} = \nu_{13} = 0.25, \nu_{23} = 0.45 \\
 \mathcal{L} &= 100 \text{ mm}, a_0 = 40 \text{ mm}, 2h = 3 \text{ mm}, B = 10 \text{ mm} \\
 \sigma_n^0 &= 60 \text{ MPa}, \sigma_t^0 = 80 \text{ MPa}
 \end{aligned}
 \tag{58}$$

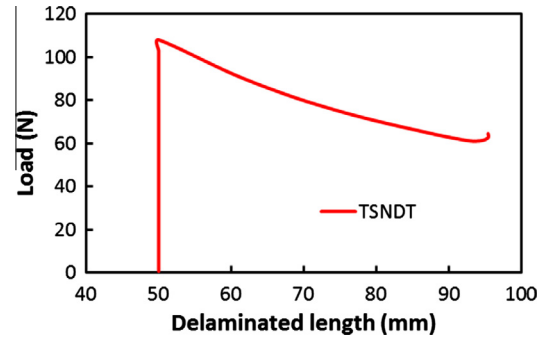


Fig. 12. Load P_3^t vs. delaminated length, $\sigma_t^0 = 80$ MPa (121 nodes).

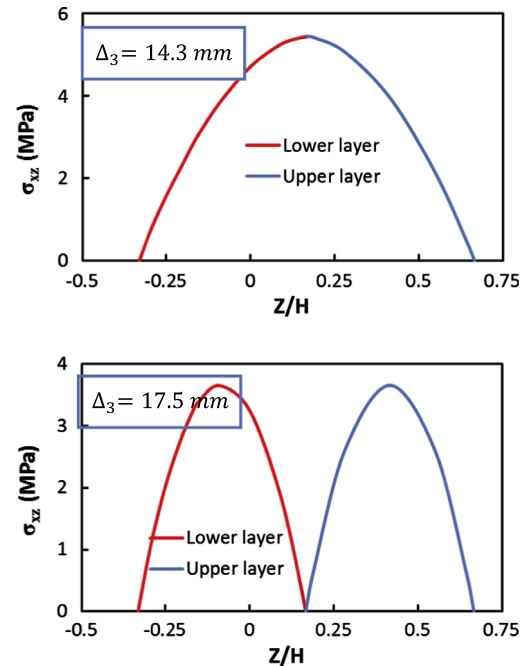


Fig. 13. Variation of σ_{xz} at $x = 40$ mm for two values of the edge displacement, Δ_3 ($H = 2$ h).

The following boundary conditions at $x = \mathcal{L}$ are imposed

$$\omega_{30}^e(\mathcal{L}) = -\Delta_3, \omega_{3i}^e(\mathcal{L}) = \omega_{3i}^b(\mathcal{L}) = 0, \quad i = 1, 2, 3 \tag{59.a}$$

$$\omega_{30}^b(\mathcal{L}) = 0, M_{11}^j(\mathcal{L}) = 0, \quad j = 1, 2, \dots, 12, \quad M_{31}^j(\mathcal{L}) = 0, \quad j = 5, 6, 7, 8 \tag{59.b, c, e}$$

We call $\bar{P}_3 = -P_3^b$ as the shear load. In Fig. 16 we have compared the presently computed load (\bar{P}_3)-edge displacement (Δ_3) curve with those of Ref. [21] for $\beta = 1$ and 2 in Eq. (20). The presently computed peak value of the shear load differs from that of [21] by 9.1% and 8.6% for $\beta = 1$ and 2, respectively. It is clear that the value of β in Eq. (20) affects the load when the delamination initiates. The ratio of G_I/G_{II} vs. the delamination length shown in Fig. 17 is nearly constant and equals 1.35 which agrees with the analytical result of [7]. Values of G_I and G_{II} are calculated from Eq. (24).

4.2. Delamination in quasistatic deformations of linear elastic curved beam

We now study delamination growth in mode-I deformations of a linear elastic, homogeneous and isotropic curved beam shown in Fig. 18 that have been studied by Guedes et al. [23] and compare

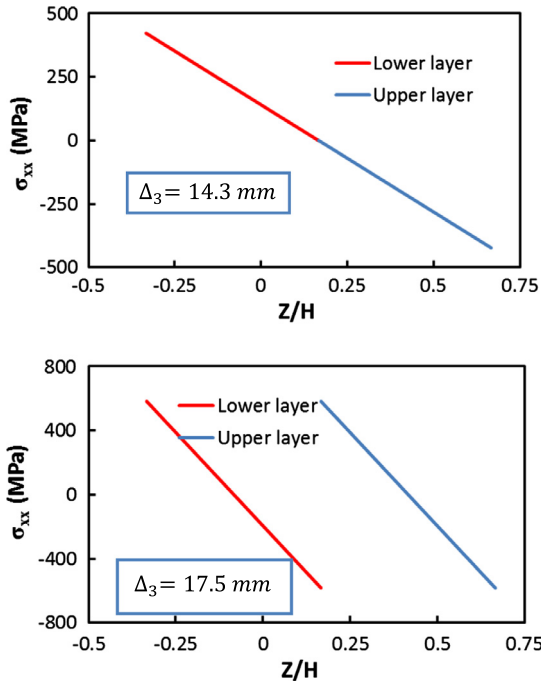


Fig. 14. Variation of σ_{xx} at $x = 40$ mm for two values of the edge displacement, Δ_3 ($H = 2$ h).

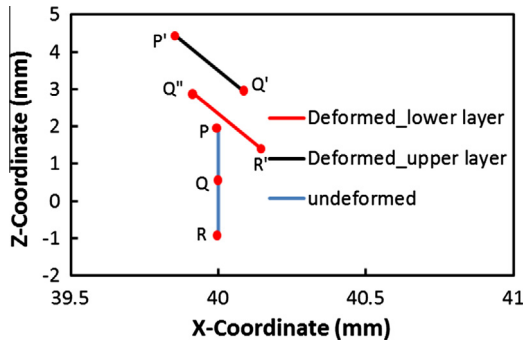


Fig. 15. For $\Delta_3 = 17.5$ mm, deformed configurations of a line initially perpendicular to the centroidal axis at $x = 40$ mm (121 nodes).

our results with those of [23]. The beam is deformed by applying displacements $\Delta_3^t = -\Delta_3^b = \Delta_3$ at points on the right edge. Values of the material and the geometric parameters used to compute results are listed below.

$$\begin{aligned}
 E_1 &= 4.5 \text{ GPa}, G_{13} = 1.0 \text{ GPa}, E_2 = E_3 = 1.7 \text{ GPa}, \nu_{12} = \nu_{13} = 0.3, \\
 \nu_{23} &= 0.4 \\
 G_{Ic} &= 800 \text{ Jm}^{-2}, G_{IIc} = 1200 \text{ Jm}^{-2}, \sigma_n^0 = \sigma_t^0 = 20 \text{ MPa} \\
 \theta_T &= 0.182\pi, \theta_D = 0.063\pi, 2h = 11.6 \text{ mm}, B = 22.8 \text{ mm}, R = 40 \text{ h}
 \end{aligned}
 \tag{60}$$

Here θ_T is the central angle of the entire beam, θ_D the central angle of the initially delaminated part of the beam, and R is the mid-surface radius. Boundary conditions for this problem are identical to those of the problem studied in Section 4.1.1.

The presently computed load (P_3^t) vs. end displacement (Δ_3^t) curve shown in Fig. 19 agrees well with that of [23]. The two FE meshes with 81 and 121 nodes give basically the same P_3^t vs. Δ_3^t curves, the presently computed peak load differs from that of Ref. [23] by 4.1% and the two end displacements when the peak

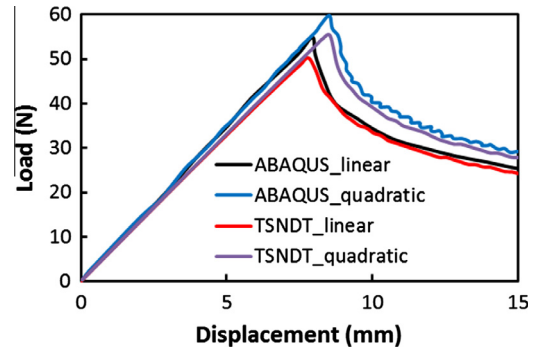


Fig. 16. Comparison of the presently computed load (\bar{P}_3)-edge displacement (Δ_3) curves for mixed-mode deformations using linear ($\beta = 1$) and quadratic ($\beta = 2$) fracture energy criteria (cf. Eq. (20)) with those of ABAQUS reported in [21] ($\sigma_n^0 = 60$ MPa, 121 nodes).

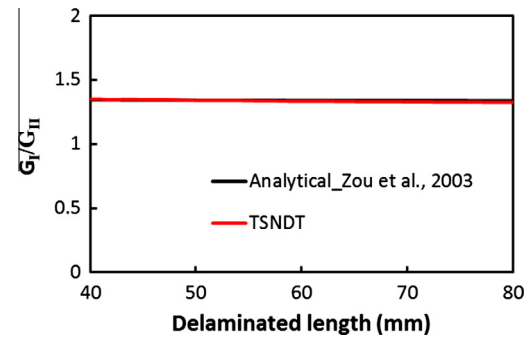


Fig. 17. Mode-mixity ratio vs. the delaminated length for mixed-mode deformations using $\sigma_n^0 = 60$ MPa.

loads occur differ by 1.3%. The load vs. the delaminated length curve exhibited in Fig. 20 indicates that the load monotonically decreases with an increase in the delamination length. The variation with Δ_3^t of the strain energy W_e stored in the beam, the work done by external forces and the energy dissipated during delamination, displayed in Fig. 21, reveal that the maximum difference $100(W_p - W_e - W_d)/W_p$ equals 0.6% signifying that the balance of energy is well satisfied.

4.3. Delamination growth in mode-I deformations of straight DCB with consideration of all geometric nonlinearities

We study the same problem as that analyzed by Allix and Corigliano [11]. Whereas they used the displacement field of the Timoshenko beam theory we use that of the TSNDT. We note that the Timoshenko beam theory neglects transverse normal strains and assumes the transverse shear strain to be constant. However, the geometrically nonlinear TSNDT assumes quartic variation through-the-thickness of the transverse normal strain and quintic variation of the transverse shear strain. Values assigned to the material and the geometric parameters taken from Ref. [11] are listed below.

$$\begin{aligned}
 E_1 &= 135 \text{ GPa}, G_{13} = 5.7 \text{ GPa}, E_2 = E_3 = 10.0 \text{ GPa} \\
 \nu_{12} &= \nu_{13} = 0.3, \nu_{23} = 0.3, G_{Ic} = 400 \text{ Jm}^{-2} \\
 \mathcal{L} &= 20 \text{ mm}, a_0 = 5.5 \text{ mm}, 2h = 0.4 \text{ mm}, B = 1 \text{ mm}, \sigma_n^0 = 20 \text{ MPa}.
 \end{aligned}
 \tag{61}$$

Values of E_2, E_3 and Poisson's ratios are not given in [11], and have been estimated in the present work. Boundary conditions for this problem are listed as Eq. (54).

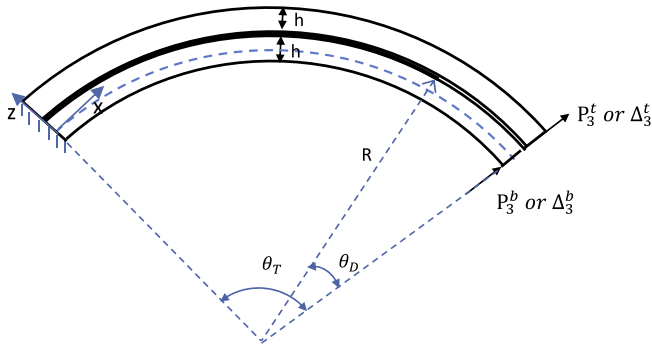


Fig. 18. Curved DCB clamped at the left end and loaded by applying radial displacements at the right end.

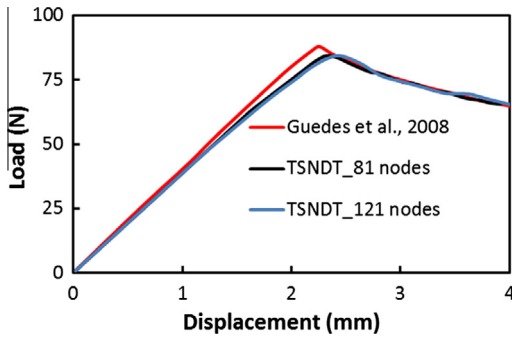


Fig. 19. Load (P_3^t)-right edge displacement (Δ_3^t) curves for the curved beam of Fig. 18.

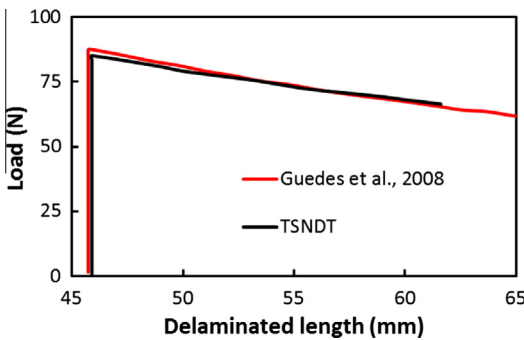


Fig. 20. Load (P_3^t) vs. delaminated length (121 nodes) for the curved beam of Fig. 18.

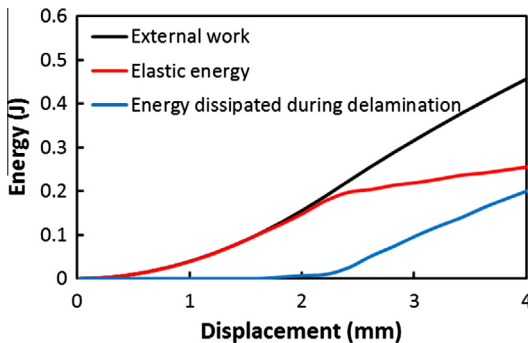


Fig. 21. For the curved beam of Fig. 18, variation with the right edge displacement of the work done by external forces, strain energy stored in the beam and energy dissipated during delamination (121 nodes).

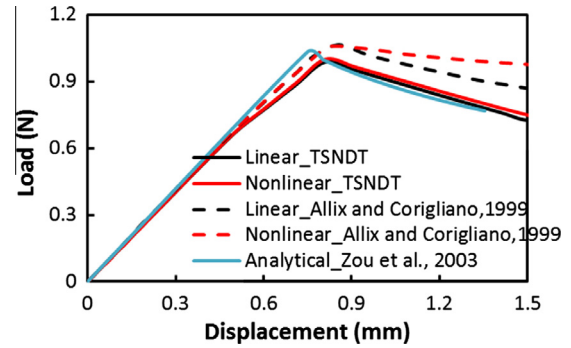


Fig. 22. For mode-I deformations of the DCB, comparison of load (P_3^t) vs. the edge displacement (Δ_3^t) curves for the linear and the nonlinear analyses using 81 nodes.

From the load (P_3^t) vs. the edge displacement (Δ_3^t) curves plotted in Fig. 22, we conclude that the presently computed peak loads for the linear and the nonlinear problems are essentially equal to each other. However, for $\Delta_3^t = 1.5$ mm, the presently computed load from the nonlinear analysis exceeds that from the linear analysis by about 3%. Whereas delamination initiates for the same value of Δ_3^t for the Timoshenko beam theory used by Allix and Carigliano [11] and the TSNDT used here, the two peak loads differ by 5.9%. For deformations subsequent to the initiation of delamination the P_3^t vs. Δ_3^t curves from the present work are close to that from the analytical solution of Zou et al. [7] based on the linear theory but differ noticeably from those reported by Allix and Corigliano [11].

4.4. Post-buckling deformations of pre-delaminated beam deformed in axial compression

Pre- and post-buckling deformations of an initially debonded [0₄/0₁₂/0₄] beam shown in Fig. 23a and analyzed in [24] are simulated considering all geometric nonlinearities. The initial debonded length located at the mid-span between the top face sheet and the core equals a_1 . The nonsymmetrical perturbation shown in Fig. 23a with $P_0 = 0.01$ N is applied, and the beam with the right edge clamped is deformed by applying axial displacement Δ_1 on the left edge in increments of 0.001 mm. Thus

$$\begin{aligned} \alpha_{3i}^c(0) = \alpha_{3i}^b(0) = \alpha_{3i}^t(0) = 0, \quad i = 0, 1, 2, 3 \\ \alpha_{1i}^c(0) = \alpha_{1i}^b(0) = \alpha_{1i}^t(0) = 0, \quad i = 1, 2, 3 \\ \alpha_{10}^b(0) = \alpha_{10}^t(0) = 0, \quad \alpha_{10}^c(0) = \Delta_1 \end{aligned} \quad (62.a)$$

The point load P_0 at $(\mathcal{L}/2, H/2)$ is replaced by the surface traction $T_{31}(x, H/2) = (P_0/\varepsilon)\delta(\mathcal{L}/2 - \varepsilon/2, H/2)$ where $\delta(x, H/2)$ is the delta function centered at $(x, H/2)$.

The compressive axial load P is found by integrating $T_{11}(0, z)$ over the thickness, multiplying the result with the beam width, and taking the absolute value. Values of the geometric and the material parameters taken from [24] are

$$\begin{aligned} E_1 = 139.3 \text{ GPa}, G_{13} = 5.58 \text{ GPa}, E_2 = E_3 = 9.72 \text{ GPa}, \nu_{12} = \nu_{13} = 0.29, \nu_{23} = 0.4 \\ G_{1c} = 87.6 \text{ Jm}^{-2}, G_{IIc} = 315.2 \text{ Jm}^{-2}, \sigma_n^0 = 44.54 \text{ MPa}, \sigma_t^0 = 106.9 \text{ MPa} \\ \mathcal{L} = 50.8 \text{ mm}, a_1 = 19.05 \text{ mm}, H = 2.59 \text{ mm}, B = 5.08 \text{ mm} \end{aligned} \quad (63)$$

The presently computed results are compared with the numerical solution of [24] and the experimental findings of [25]. In Figs. 24 and 25 we have exhibited the axial load vs. the engineering axial strain, and the axial load vs. the mid-span deflections (or z -displacements) of the top and the bottom surfaces. Results computed with two FE meshes having 120 and 160 two-node elements are close to each other. The drop in the axial load at an axial strain of about 0.25% indicates that the delamination begins to propagate. The value of this load for the 121-node mesh exceeds that for the

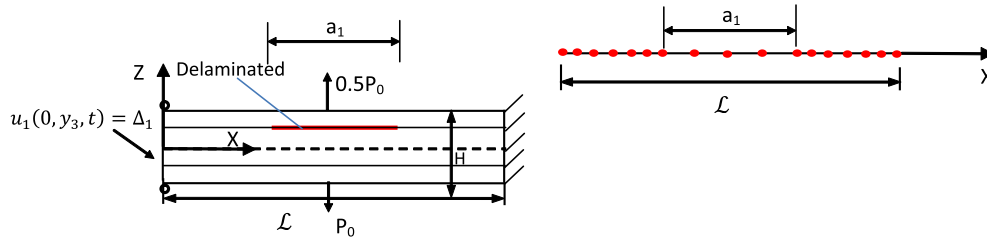


Fig. 23. (a) Sketch of initially delaminated beam deformed in uniaxial compression, unequal perturbations applied at the top and the bottom surfaces, and sketch of the FE mesh (not to scale).

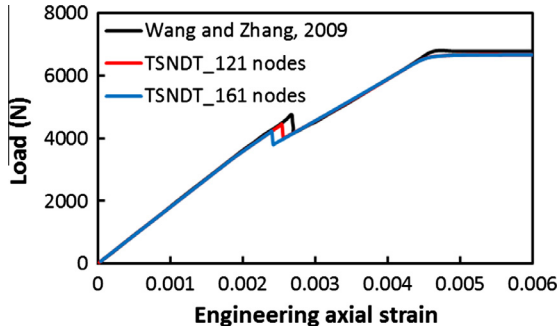


Fig. 24. Axial compressive load P vs. the engineering axial strain.

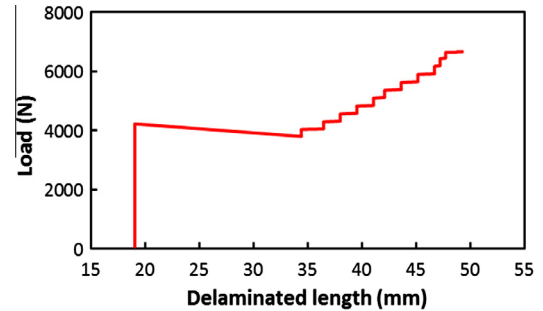


Fig. 26. Axial compressive load P vs. delaminated length during axial compression of an initially delaminated composite beam.

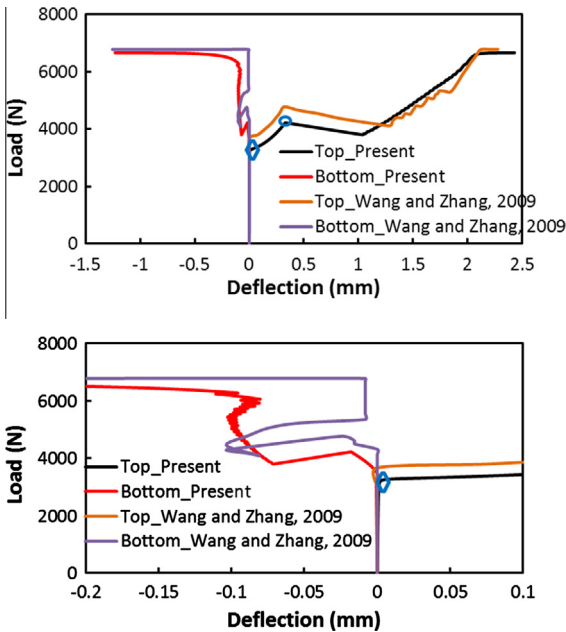


Fig. 25. Axial compressive load P vs. the mid-span deflection of the top and the bottom surfaces, symbol \diamond represents the local buckling load (3404 N), symbol \circ represents the load (4226 N) when the delamination begins to propagate. A blown-up view of the plot for the deflection varying between -0.2 and 0.1 mm is shown in the bottom figure.

161-node mesh by 5.0%, and the corresponding values of the axial strains differ by 5.6%. The axial load and the axial strain for the 161-node mesh at the instant of delamination propagation differ from the corresponding values reported by Wang and Zhang [24] by 11% and 10%, respectively.

Whereas the presently computed axial load vs. the axial engineering strain curve is close to that of Ref. [24], the axial load vs. the mid-span deflection curves exhibited in Fig. 25 show some deviations. With an increase in the axial compression, the upper

sub-laminate buckles locally and its mid-span deflection increases significantly. The initiation of local buckling at an axial load of 3.4 kN is indicated by the symbol \diamond . With continued axial compression, both the axial load and the lateral deflections of the top and the bottom surfaces monotonically increase till delamination begins to propagate between the top layer and the core. As should be clear from the plot of the axial load vs. the delaminated length exhibited in Fig. 26, the axial load slowly decreases from 4.2 kN with an increase in the delaminated length, and the delamination is unstable till the delaminated length equals about 34.4 mm. Subsequently, the axial load increases even though more of the interface is being delaminated which indicates stable delamination growth.

The lower sub-laminate begins to buckle when the load reaches the collapse load of 6.7 kN. The difference between the presently computed collapse load and that reported in [24] is 1.55%. However, both these values exceed the experimental value [25] of the collapse load by about 24% as should be clear from the variation of the axial load with the axial strain at the mid-span of the top surface displayed in Fig. 27. One reason for this difference is the failure of the material near the clamped ends not considered in the studies. The initiations of local buckling and unstable delamination growth agree with the experimental results of [25] except that we overestimate the collapse load.

Variations with the axial strain of the strain energy stored in the beam, the work done by external forces and the energy dissipated due to delamination are exhibited in Fig. 28. The total energy dissipated during delamination is only about 4% of the work done by external forces which is mostly stored as strain energy in the beam. We have plotted in Fig. 29 the deformed shapes of laminated beam corresponding to two values of the axial compressive strain.

4.5. Transient deformations

4.5.1. Transient deformations of DCB

We study delamination growth in dynamic mode-II deformations of the beam studied in subsection 4.1.3, take mass density

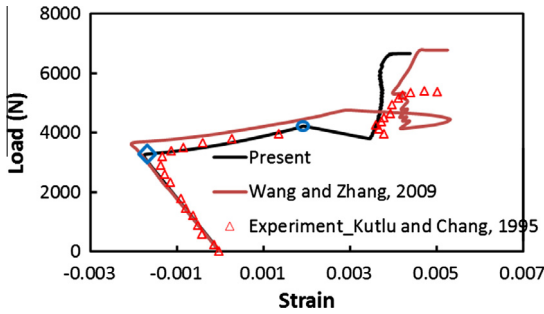


Fig. 27. Axial compressive load P vs. axial engineering strain, du/dx , at the mid-span of the top surface of the beam, symbol \diamond represents the local buckling load (3404 N), and symbol \circ represents the load when the delamination begins to propagate (4226 N).

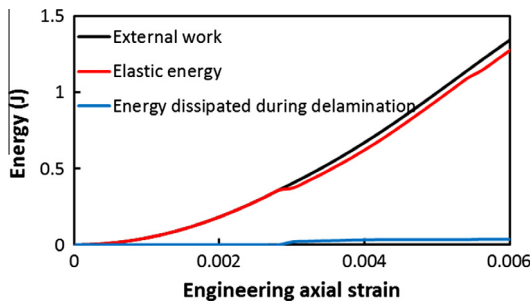


Fig. 28. Variation with the engineering axial strain of the work done by external forces, strain energy stored in the beam, and the energy dissipated during delamination.

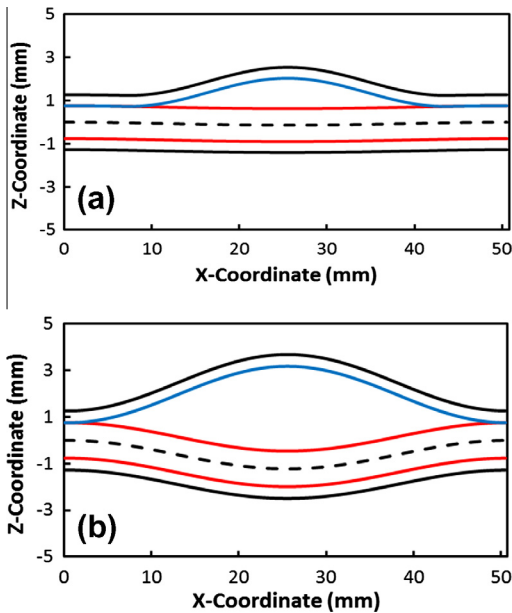


Fig. 29. Deformed shapes of the beam corresponding to engineering axial strain of (a) 0.33% and (b) 0.6%.

equal to 2000 kg/m^3 , employ the same FE mesh (121 nodes) as that used in Section 4.1.3, neglect effects of geometric nonlinearities, and compute results for $\Delta_3 = 2.5 \text{ m/s}$ and 0.25 m/s . The load (P_3)-displacement (Δ_3) curves plotted in Fig. 30 reveal that inertial ef-

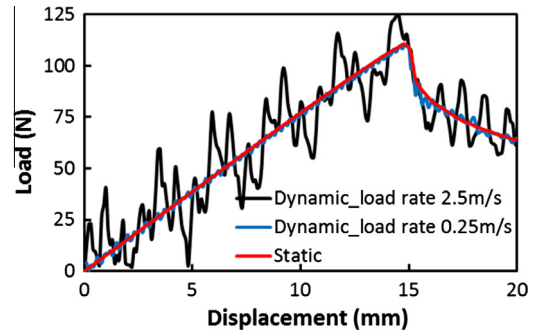


Fig. 30. Load P_3 vs. edge displacement Δ_3 curves for mode-II deformations with $\Delta_3 = 0.25$ and 2.5 m/s (121 nodes).

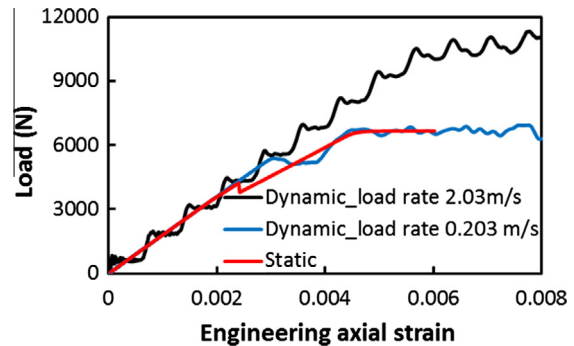


Fig. 31. Axial compressive load P vs. engineering axial strain for $\Delta_1 = 0.203$ and 2.03 m/s .

fects are insignificant for $\Delta_3 = 0.25 \text{ m/s}$, and $\Delta_3 = 2.5 \text{ m/s}$ results in oscillatory P_3 - Δ_3 curve suggesting that inertial effects are noticeable. The peak load for the transient problem with $\Delta_3 = 2.5 \text{ m/s}$ is about 14% higher than that for the static problem. The time step used to compute results found by using the criterion discussed in Section 3.3 equaled 8 ns.

4.5.2. Dynamic post-buckling deformations of pre-delaminated beam deformed in axial compression

We delineate the effect of inertia forces on post-buckling deformations of an initially debonded beam deformed in axial compression by restudying the problem of subsection 4.4 using the FE mesh with 121 nodes, taking mass density = 2000 kg/m^3 , and $\Delta_1 = 2.03$ and 0.203 m/s or equivalently axial strain rates of 40 and 4/s, respectively. Results were computed with $\Delta t = 14 \text{ ns}$. The axial load vs. the engineering axial strain curves displayed in Fig. 31 reveal that, for $\Delta_1 = 2.03 \text{ m/s}$, the consideration of inertia effects increases the buckling load from 6.1 kN for the static analysis to 10.5 kN for the dynamic problem, i.e., by about 65%. Thus the dynamic load amplification factor (DLAF) equals 1.65. Batra and Geng [26] found that for a pinned-pinned column the DLAF varied from 1.69 to 8.59 when loading rate was increased from 20 to 1000 kN/s.

Variations of the axial compressive load P vs. the delaminated length for the two loading rates are shown in Fig. 32. The load corresponding to the initiation of the unstable delamination growth increases with an increase in the loading rate, it equals 4.2, 5.5 and 10.5 kN for the quasistatic problem, $\Delta_1 = 0.203 \text{ m/s}$ and $\Delta_1 = 2.03 \text{ m/s}$, respectively. The delaminated length that grows unstably changes from about 15 mm for the quasistatic problem to 32 and 25 mm for $\Delta_1 = 0.203$ and 2.03 m/s , respectively. We recall that results have been computed by prescribing displacements at the end faces.

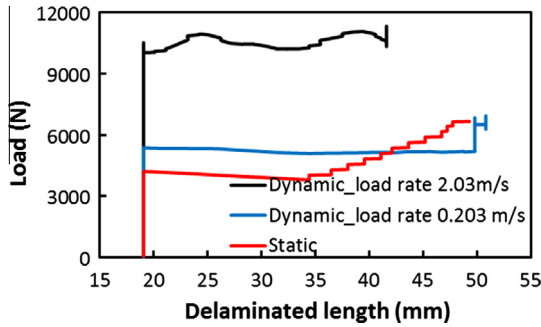


Fig. 32. Axial compressive load P vs. delaminated length for $\Delta_1 = 0.203$ and 2.03 m/s.

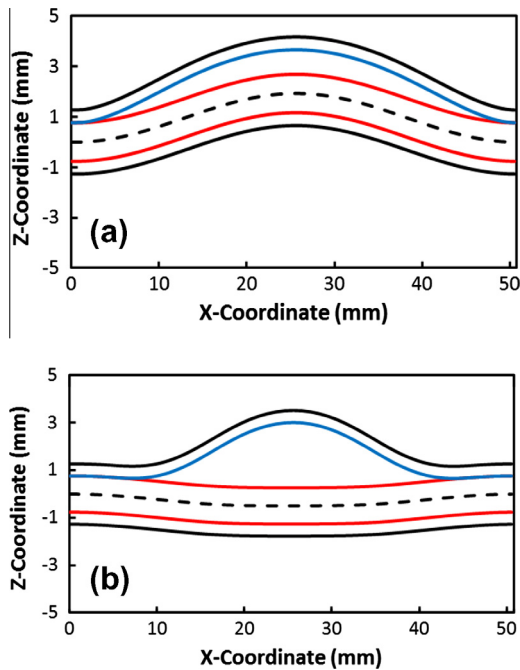


Fig. 33. At an engineering axial strain of 0.8%, deformed shapes of the beam for (a) $\Delta_1 = 0.203$ m/s, and (b) $\Delta_1 = 2.03$ m/s.

Fig. 33 shows deformed shapes of the beam for different loading rates when the engineering axial strain equals 0.8%. Whereas delamination propagated to the ends of the beam for $\Delta_1 = 0.203$ m/s, it did not propagate to the end faces of the beam for $\Delta_1 = 2.03$ m/s because the beam buckled globally. In Fig. 34 we have plotted variation with the engineering axial strain of the mid-span deflections of the top and the bottom surfaces of the beam. These results suggest that an increase in the loading rate smoothens out the rate of increase of deflections of the two surfaces. The unstable growth of delamination could not be detected by studying the growth in the deformed shapes of the top and the bottom surfaces.

We note that the TSNDT discussed here generalizes the higher-order shear and normal deformable plate theory of Batra and Vidoli [27] to finite deformations. Several plate problems for linear elastic materials using the Batra and Vidoli plate theory have been discussed in Refs. [28–31], and exact solutions for plate deformations are given in Refs. [32,33]. Recently, Thai et al. [34] and Kapoor and Kapania [35], amongst others, have used the isogeometric basis functions and a layer-wise first-order shear deformation theory to analyze several problems for plates.

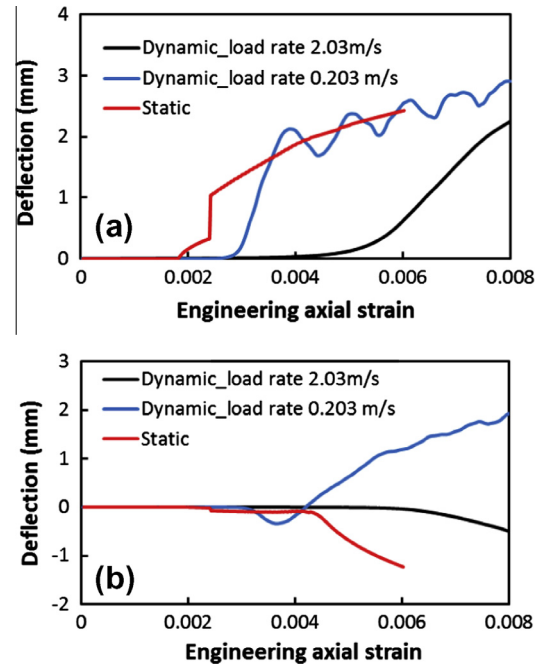


Fig. 34. For $\Delta_1 = 0.203$ and 2.03 m/s, variation with the engineering axial strain of the mid-span deflection of (a) the top, and (b) the bottom surfaces.

5. Conclusions

We have used a cohesive zone model (CZM) and a layer-wise third-order shear and normal deformable beam theory (TSNDT) to analyze delamination growth in a laminated composite beam, and compared our results with those available in the literature for nine problems. We have considered all geometric nonlinearities including the von Karman nonlinearity. Presently computed results for mode-I, mode-II and mixed-mode deformations of straight and curved cantilever beams under the assumption of infinitesimal deformations have been found to agree well with those of other investigators including results obtained using the linear elastic fracture mechanics approach. During the analysis of delamination growth in axial compression of an initially delaminated beam we found that local buckling ensues first and it is followed by global buckling. Because of the geometric nonlinearities considered, we could also analyze the post-buckling response of the beam which is found to agree well with experimental results reported in the literature. We have also studied the effect of inertia forces on delamination growth in a pre-delaminated beam. It is found that for the applied axial strain rate of 40/s, the buckling load increases by 65% over that for the static problem, and the length of the unstably grown delaminated region decreases by 30%.

Acknowledgements

This work was supported by the Office of Naval Research Grant N00014-11-1-0594 to Virginia Polytechnic Institute and State University with Dr. Y.D.S. Rajapakse as the Program Manager. Views expressed in the paper are those of the authors and neither of the funding agency nor of authors' Institution.

References

- [1] Irwin GR. Analysis of stresses and strains near the end of a crack traversing a plate. *J Appl Mech* 1957;24:361–4.
- [2] Rice JR. A path independent integral and the approximate analysis of strain concentration by notches and cracks. DTIC Document; 1967.
- [3] Hellen TK. On the method of virtual crack extensions. *Int J Numer Meth Eng* 1975;9(1):187–207.

- [4] Needleman A. A continuum model for void nucleation by inclusion debonding. *J Appl Mech* 1987;54(3):525–31.
- [5] Mi Y, Crisfield MA, Davies GAO, Hellweg HB. Progressive delamination using interface elements. *J Compos Mater* 1998;32(14):1246–72.
- [6] Tvergaard V, Hutchinson JW. The relation between crack growth resistance and fracture process parameters in elastic–plastic solids. *J Mech Phys Solids* 1992;40(6):1377–97.
- [7] Zou Z, Reid S, Li S. A continuum damage model for delaminations in laminated composites. *J Mech Phys Solids* 2003;51(2):333–56.
- [8] Camanho PP, Dávila CG. Mixed-mode decohesion finite elements for the simulation of delamination in composite materials. NASA-Technical Paper, 2002. 211737.
- [9] Balzani C, Wagner W. An interface element for the simulation of delamination in unidirectional fiber-reinforced composite laminates. *Eng Fract Mech* 2008;75(9):2597–615.
- [10] Xie D, Waas AM. Discrete cohesive zone model for mixed-mode fracture using finite element analysis. *Eng Fract Mech* 2006;73(13):1783–96.
- [11] Allix O, Corigliano A. Geometrical and interfacial non-linearities in the analysis of delamination in composites. *Int J Solids Struct* 1999;36(15):2189–216.
- [12] Zhang Y, Wang S. Buckling, post-buckling and delamination propagation in debonded composite laminates: part 1: theoretical development. *Compos Struct* 2009;88(1):121–30.
- [13] Batra RC, Xiao J. Finite deformations of curved laminated St. Venant–Kirchhoff beam using layer-wise third order shear and normal deformable beam theory (TSNDT). *Compos Struct* 2013;97:147–64.
- [14] Saada AS. *Elasticity: theory and applications*. Malabar, FL: Krieger; 1993.
- [15] Batra RC. *Elements of continuum mechanics*. AIAA; 2006.
- [16] Qian LF, Batra RC. Three-dimensional transient heat conduction in a functionally graded thick plate with a higher-order plate theory and a meshless local Petrov–Galerkin method. *Comput Mech* 2005;35(3):214–26.
- [17] Xiao JR, Gilhooley DF, Batra RC, Gillespie JW, McCarthy MA. Analysis of thick composite laminates using a higher-order shear and normal deformable plate theory (HOSNDPT) and a meshless method. *Compos Part B: Eng* 2008;39(2):414–27.
- [18] Hashemi S, Kinloch AJ, Williams JG. The analysis of interlaminar fracture in uniaxial fibre–polymer composites. *Proc R Soc Lond A. Math Phys Sci* 1990;427(1872):173–99.
- [19] De Moraes AB, De Moura MFSF. Evaluation of initiation criteria used in interlaminar fracture tests. *Eng Fract Mech* 2006;73(16):2264–76.
- [20] Chen J, Crisfield M, Kinloch A, Busso E, Matthews F, Qiu Y. Predicting progressive delamination of composite material specimens via interface elements. *Mech Compos Mater Struct* 1999;6(4):301–17.
- [21] Goyal VK, Johnson ER, Dávila CG. Irreversible constitutive law for modeling the delamination process using interfacial surface discontinuities. *Compos Struct* 2004;65(3):289–305.
- [22] Pearson RA, Blackman BR, Campilho RD, de Moura MF, Dourado NM, Adams RD, et al. Quasi-static fracture tests. testing adhesive joints. *Best Practices* 2012; p. 163–271.
- [23] Guedes RM, Sá A, De Moura M. An experimental and numerical assessment of DCB tests on glass/polyester curved beams cut out from pipes. *Polymer Test* 2008;27(8):985–94.
- [24] Wang S, Zhang Y. Buckling, post-buckling and delamination propagation in debonded composite laminates part 2: numerical applications. *Compos Struct* 2009;88(1):131–46.
- [25] Kutlu Z, Chang FK. Composite panels containing multiple through-the-width delaminations and subjected to compression. Part II: experiments & verification. *Compos Struct* 1995;31(4):297–314.
- [26] Batra RC, Geng TS. Enhancement of the dynamic buckling load for a plate by using piezoceramic actuators. *Smart Mater Struct* 2001;10(5):925–33.
- [27] Batra RC, Vidoli S. Higher order piezoelectric plate theory derived from a three-dimensional variational principle. *AIAA J* 2002;40(1):91–104.
- [28] Batra RC, Vidoli S, Vestroni F. Plane waves and modal analysis in higher-order shear and normal deformable plate theories. *J Sound Vibration* 2002;257(1):63–88.
- [29] Batra RC, Aimmanee S. Vibrations of thick isotropic plates with higher order shear and normal deformable plate theories. *Comput Struct* 2005;83:934–55.
- [30] Qian LF, Batra RC, Chen LM. Free and forced vibrations of thick rectangular plates by using higher-order shear and normal deformable plate theory and meshless Petrov–Galerkin (MLPG) method. *Comput Model Eng Sci* 2003;4:519–34.
- [31] Xiao JR, Gilhooley DF, Batra RC, Gillespie Jr JW, McCarthy MA. Analysis of thick composite laminates using a higher-order shear and normal deformable plate theory (HOSNDPT) and a meshless method. *Composites B* 2008;39:414–27.
- [32] Vel S, Batra RC. Analytical solutions for rectangular thick laminated plates subjected to arbitrary boundary conditions. *AIAA J* 1999;37:1464–73.
- [33] Vel SS, Batra RC. The generalized plane strain deformations of thick anisotropic composite laminated plates. *Int J Solids Struct* 2000;37:715–33.
- [34] Thai CH, et al. Isogeometric analysis of laminated composite and sandwich plates using a layerwise deformation theory. *Compos Struct* 2013, <http://dx.doi.org/10.1016/j.compstruct.2013.04.002>.
- [35] Kapoor H, Kapania RK. Geometrically nonlinear NURBS isogeometric analysis of laminated composite plates. *Compos Struct* 2012;94:3434–47.